Environmental Science Advances

ROYAL SOCIETY OF CHEMISTRY

CRITICAL REVIEW

View Article Online
View Journal | View Issue

Cite this: *Environ. Sci.: Adv.*, 2026, **5**, 369

Magnetic graphene nanocomposites: a new frontier in radioactive waste remediation

M. Mahiuddin, *[a] Abhijit Barua, [b] A. B. M. Nazmul Islam, [a] M. Saiful Islam Monir, [a] Abdur Rahman,[a] Samir Mallick, [c] Joshua T. Moore, [c] Tasneem A. Siddiquee, [c] Zinnat Rahman [d] and Ismail Rahman *[d]

The management of radioactive waste presents formidable environmental and health challenges, necessitating the development of effective remediation technologies. Magnetic nanocomposites (NCs) derived from iron oxide (Fe_3O_4) and graphene derivatives have emerged as highly promising materials for the sorptive removal of radionuclides from contaminated aqueous streams. This comprehensive review critically examines the synthesis, characterization, and application of these NCs. The key physicochemical properties—including structural, magnetic, and surface characteristics—that underpin their high sorption capacities have been explored. The discussion covers various synthesis methodologies and the analytical techniques used to validate the properties of the materials. A central focus is placed on the sorption mechanisms, performance efficiency, and the operational factors influencing the sequestration of radioactive ions. Despite their significant potential, several challenges related to scalability, long-term stability, selective sorption in complex matrices, and potential environmental impacts have been identified and discussed. Finally, future research directions to advance the practical application of Fe_3O_4@graphene NCs in radioactive waste management have been discussed. This review provides a foundational understanding of the capabilities and limitations of these materials, aiming to guide future research toward their practical implementation in mitigating the hazards of radioactive contamination.

Received 10th September 2025
Accepted 7th January 2026

DOI: 10.1039/d5va00319a

rsc.li/esadvances

Environmental significance

Radioactive contamination from nuclear activities poses a severe and persistent threat to ecosystems and human health. This work reviews the significant advancements in magnetic graphene nanocomposites as a superior alternative to conventional approaches for radionuclide removal from contaminated water. These nanomaterials exhibit high sorption capacity and can be easily separated from water using a magnetic field, allowing for efficient reuse. The technology offers a transformative approach to radioactive waste management, providing an effective and sustainable solution to mitigate the long-term environmental hazards of nuclear contamination, thereby protecting natural environments and safeguarding public health from the risks of radiation exposure.

1.0 Introduction

The proliferation of anthropogenic radionuclides in the environment represents a persistent and insidious global threat. Arising from historical nuclear weapons testing and both routine and accidental releases from the expanding global network of nuclear facilities, these contaminants pose a long-term risk to ecosystems and human health.[1–6] Catastrophic events, such as those at Kyshtym (1957), Chornobyl (1986), and Fukushima Daiichi (2011), serve as stark reminders of the potential for widespread and lasting environmental contamination.[6–9] Compounding this issue is the vast accumulation of legacy radioactive waste in nations with established nuclear programs, including the United States, Russia, and the United Kingdom.[2,3] Once released, radionuclides can enter the food chain, where they bioaccumulate and biomagnify, posing a severe radiological risk to human health even from initially trace concentrations.[4,6,10–12]

Consequently, the safe and effective management of radioactive waste has become a paramount challenge at the intersection of nuclear technology, environmental science, and materials chemistry.[13–17] The extreme longevity of many radionuclides, which can remain hazardous for millennia, necessitates containment strategies that are not only robust but also sustainable over geological timescales.[11,18,19] Traditional

[a]*Chemistry Discipline, Khulna University, Khulna 9208, Bangladesh. E-mail: mahiuddin@chem.ku.ac.bd*

[b]*Graduate School of Symbiotic Systems Science and Technology, Fukushima University, 1 Kanayagawa, Fukushima-shi, Fukushima 960-1296, Japan*

[c]*Department of Chemistry, Tennessee State University, Nashville, TN 37209, USA*

[d]*Institute of Environmental Radioactivity, Fukushima University, 1 Kanayagawa, Fukushima City, Fukushima 960-1296, Japan. E-mail: immrahman@ipc.fukushima-u.ac.jp*

Table 1 Comparison of key remediation techniques for radioactive waste management

Technique	Action	Advantages	Disadvantages
Chemical precipitation	Converts soluble radionuclides into insoluble precipitates *via* the addition of chemical reagents	• High efficiency for high-concentration waste • Cost-effective for treating large volumes	• Generates substantial volumes of secondary radioactive sludge • Low efficiency for removing trace-level or low-concentration radionuclides
Ion exchange	Utilizes solid materials (*e.g.*, resins or zeolites) to reversibly exchange non-radioactive ions for radionuclide ions in the liquid phase	• High selectivity and removal efficiency • Effective for large volumes of low-salinity aqueous waste	• High cost of resins • Regeneration produces concentrated liquid secondary waste • Performance is susceptible to competing non-radioactive ions
Membrane separation	Employs semi-permeable barriers to separate contaminants based on size exclusion or ionic charge	• Versatile removal of particulates, colloids, and ions • Operates at ambient temperatures	• High energy consumption due to operating pressure requirements • Prone to membrane fouling, necessitating frequent maintenance • Generates concentrated retentate streams requiring further treatment
Sorption	Uses porous solid materials (*e.g.*, graphene nanocomposites) to capture and bind radioactive ions from solution	• Minimal sludge generation compared to precipitation • Superior for "polishing" effluents with trace radionuclide concentrations (<1 ppm) • Rapid kinetics and energy-efficient separation • Amenable to regeneration or immobilization for long-term safe disposal	• Challenges in maintaining selectivity in complex matrices containing competing ions • Finite sorption capacity requires periodic regeneration or replacement of the sorbent

immobilization techniques, such as vitrification and cementation, are energy-intensive and designed primarily for high-level waste. They are often limited by high operational costs, process inefficiencies, and a lack of versatility in treating the large volumes of low-level, chemically diverse contaminated water generated by nuclear reactors, medical isotope production, and industrial applications.[4,16,20,21]

Chemical precipitation, ion exchange, membrane separation, and sorption are considered key remediation techniques for radionuclide removal.[22–24] A detailed comparison of these methods clearly articulates the scientific rationale for sorption's superiority, particularly its efficacy in polishing effluent streams and minimizing secondary waste (Table 1).

In response to these limitations, advanced materials science offers a promising paradigm shift, moving from passive containment to active treatment and removal.[6,11,19,25–27] Among the various innovations, magnetic nanocomposites (NCs) have received significant attention for their unique multifunctional properties, including exceptionally high specific surface area, robust mechanical strength, and, critically, facile separation from solution *via* an external magnetic field.[16,25,26,28] Specifically, NCs that integrate the magnetic responsiveness of iron oxide (Fe_3O_4) nanoparticles (NPs) with the unparalleled surface properties of graphene derivatives have demonstrated exceptional potential for the sorption and immobilization of radioactive contaminants. This efficacy stems from a powerful synergy: the graphene scaffold provides a vast, functionalizable

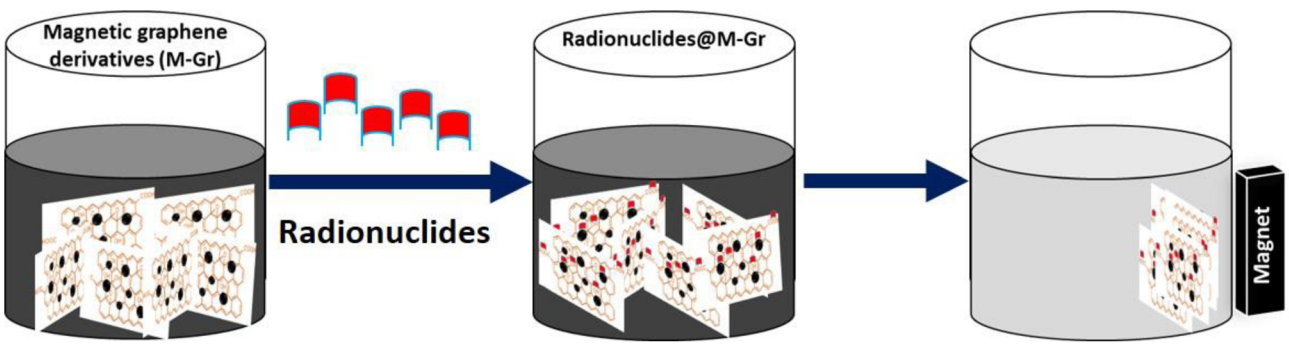

Fig. 1 Schematic diagram illustrating the process of radionuclide removal from contaminated water using magnetic graphene derivatives.

surface for radionuclide binding, while the embedded magnetic NPs enable rapid, low-energy recovery of the sorbent for reuse or safe disposal.[4,17,20,21,25,26,29–31] The fundamental principle of this magnetic separation process is depicted in Fig. 1.

This review provides a comprehensive and critical overview of recent advancements in the synthesis, characterization, and application of Fe_3O_4@graphene-based NCs for radioactive waste management. We critically evaluate the key material properties, discuss the relative merits of various synthesis methods, and detail the suite of techniques used to characterize their structure and performance. Furthermore, this review examines the mechanisms governing radionuclide sorption, candidly addresses prevailing challenges, and outlines promising future research directions. By consolidating the current state of the field, this review aims to underscore the transformative potential of Fe_3O_4@graphene NCs to improve the safety, efficiency, and sustainability of radioactive waste management practices.

2.0 Key physicochemical properties of Fe_3O_4@graphene NCs

The exceptional performance of Fe_3O_4@graphene NCs in environmental remediation stems from a unique, synergistic combination of structural, magnetic, and surface properties. These characteristics function synergistically to facilitate both effective contaminant sorption and the subsequent recovery of the sorbent material.

2.1 Structural and magnetic properties

Fe_3O_4@graphene NCs are hybrid materials formed by the intimate integration of Fe_3O_4 NPs with a graphene-based matrix, typically graphene oxide (GO) or reduced graphene oxide (rGO). The synthesis method dictates the final architecture, with Fe_3O_4 NPs—typically ranging from a few to tens of nanometers in diameter—either decorating the surface of the graphene sheets or becoming intercalated between them.[4,12,20,32–34] Within this composite structure, the Fe_3O_4 NPs critically retain their inverse spinel crystal structure, a crystallographic arrangement that is fundamental to the material's unique magnetic behavior.[4,33,35]

A defining feature of these NCs is the superparamagnetism of the Fe_3O_4 component. This phenomenon arises in magnetic NPs below a critical size, where the thermal energy is sufficient to overcome the magnetic anisotropy, causing the particle's magnetic moment to fluctuate randomly. As a result, the material exhibits zero net magnetism in the absence of an external field but becomes strongly magnetized when a field is applied.[19,29,32,33,35–39] This "on/off" magnetic behavior is essential for practical applications, as it allows for the rapid and complete recovery of the NC from aqueous solutions without the persistent particle–particle attraction (and subsequent irreversible aggregation) that would occur with permanently magnetic materials.[12,21,35,40–42]

The magnetic saturation (Ms), a measure of the maximum induced magnetic moment, is a key performance metric. While the Ms value of the NCs is invariably lower than that of pure Fe_3O_4 due to the mass contribution of the non-magnetic graphene matrix, it remains sufficiently high for efficient magnetic separation.[13,19,32,33,35–38,42,43] This strong magnetic responsiveness is a significant advantage in radioactive waste management, where minimizing processing time and ensuring complete removal of the contaminant-laden sorbent are paramount.[13,19,33,38,40] Furthermore, these composites generally exhibit high thermal and chemical stability, enabling them to function effectively across a wide range of environmental conditions, including highly acidic or alkaline environments often encountered in industrial and legacy radioactive waste streams.[12,30,36,41]

2.2 Surface area and porosity

The efficacy of any sorbent is fundamentally linked to its surface area. Graphene and its derivatives are renowned for their exceptionally high theoretical specific surface area (up to 2630 $m^2\ g^{-1}$), which provides an unparalleled platform for contaminant sorption.[3,27,44] When integrated with Fe_3O_4 NPs, the resulting NCs retain a significant portion of this high surface area. Although the incorporation of the denser Fe_3O_4 phase may lead to a reduction in the gravimetric surface area, the composite's overall surface area remains substantially larger than that of conventional sorbent materials like clays or zeolites used in radioactive waste management.[4,25] The NPs also act as spacers, preventing the graphene sheets from restacking and ensuring that the high surface area is accessible.

Experimentally, the specific surface area of Fe_3O_4@graphene NCs is commonly determined using the Brunauer–Emmett–Teller (BET) method. Measured values typically range from approximately 30 to over 400 $m^2\ g^{-1}$. This wide variation is a direct consequence of the synthesis method, the Fe_3O_4-to-graphene mass ratio, and the degree of graphene exfoliation and aggregation achieved during processing.[12,16,25,43,45,46] Beyond sheer area, the porous structure of these NCs, often featuring a hierarchical combination of micropores (<2 nm) and mesopores (2–50 nm), further enhances their sorption capacity. This hierarchical porosity is ideal for environmental applications: the larger mesopores serve as transport channels, enabling efficient diffusion of hydrated ions from the bulk solution into the material's interior, while the smaller micropores provide high-energy binding sites that contribute to strong sorption, creating a synergistic effect that improves overall performance.

2.3 Regeneration and reusability

For any sorption technology to be economically viable and environmentally sustainable, the sorbent material must be capable of regeneration and reuse. The robust covalent and non-covalent framework of Fe_3O_4@graphene NCs allows them to withstand multiple cycles of sorption and desorption without significant mechanical or chemical degradation. Adsorbed contaminants can typically be eluted by shifting the chemical equilibrium, for example, by washing with acidic solutions that protonate surface functional groups and displace bound metal cations. This process restores the active sites, enabling the material to be used in subsequent treatment cycles.[4,12,17,19–21,29,34,38,40,42,47–49]

The literature provides compelling evidence of this reusability. For instance, Zhao *et al.*[20] demonstrated that their Fe_3O_4/GO NCs retained nearly 70% of their initial U(VI) removal efficiency after five complete cycles. In another study, a similar composite maintained over 87% efficiency after five cycles using a dilute 0.1 M HCl solution for regeneration.[12] Zong *et al.*[4] reported an even more stable magnetic graphene/iron oxide composite that exhibited only a 4% decline in U(VI) sorption over seven cycles. Similarly, Yang *et al.*[49] found that their advanced GO/Fe_3O_4/GC composite retained over 85% removal efficacy for U(VI) after five cycles with regeneration using 3 M HNO_3. This high degree of reusability, combined with the low-energy, highly efficient magnetic separation process, firmly positions Fe_3O_4@graphene NCs as a promising, sustainable technological solution to the complex challenges of radioactive waste treatment.

3.0 Synthesis of Fe_3O_4@graphene NCs

The synthesis method employed to produce Fe_3O_4@graphene NCs is a critical determinant of their final physicochemical properties, including particle size distribution, morphology, surface chemistry, and magnetic responsiveness. The choice of a specific method is therefore a strategic decision based on the desired material characteristics and the intended application. This section provides a more detailed review of the most common strategies for synthesizing these advanced materials.

3.1 Simple mixing

The most direct approach to preparing these composites is to mix pre-synthesized Fe_3O_4 NPs with graphene derivatives physically. In this method, the individually prepared components are dispersed in a suitable solvent and then combined, typically under high-energy conditions such as ultrasonication or vigorous mechanical stirring, to promote the physical sorption of Fe_3O_4 NPs onto the expansive surface of the graphene sheets.[25,36,37,50,51] For example, Yang *et al.*[25] prepared their Fe_3O_4/GO NCs by simply sonicating aqueous dispersions of GO and magnetite. To overcome the limitations of weak physisorption, chemical cross-linking is often employed to create a more robust and stable composite. Fatemeh *et al.*[50] used this strategy by first functionalizing the Fe_3O_4 NPs with amine groups, which could then form strong covalent amide bonds with the carboxyl groups present on the GO surface, resulting in a highly stable final product (Fig. 2).

While this method is valued for its simplicity, inherent scalability, and versatility, it often suffers from weak van der Waals interactions between the components (in the absence of cross-linking), which can lead to NP detachment or leaching during application. Furthermore, achieving a truly homogeneous distribution of NPs on the graphene surface can be

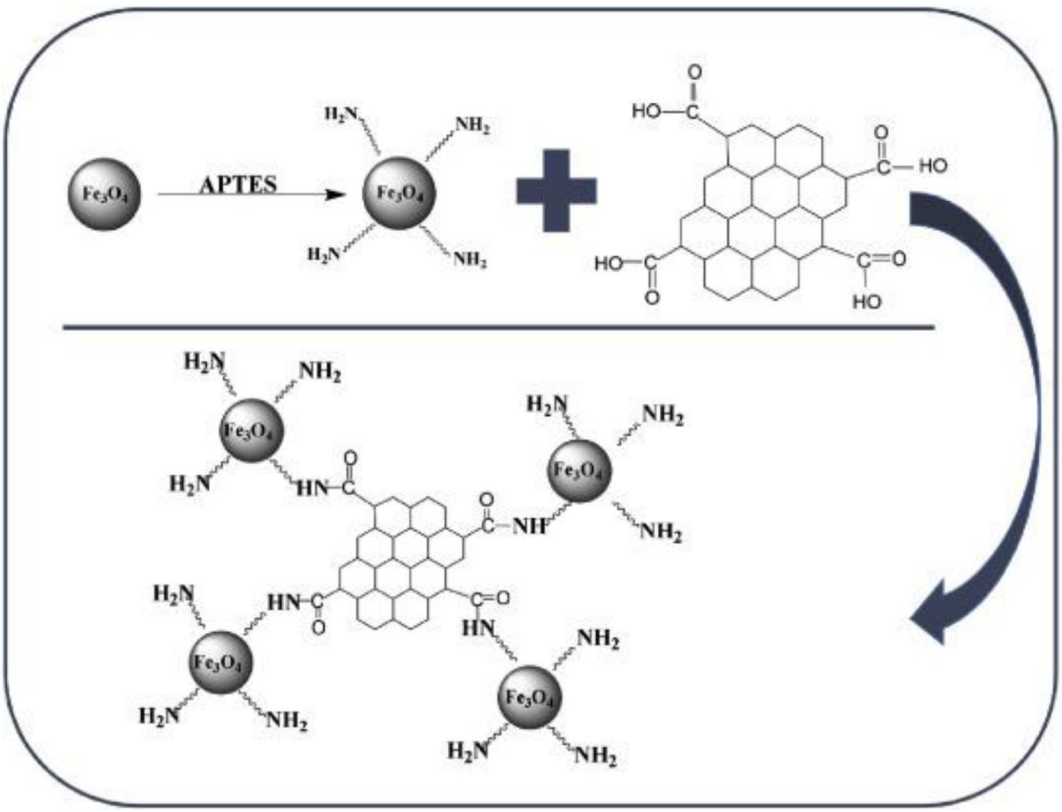

Fig. 2 Schematic representation of the synthesis of amine-functionalized Fe_3O_4/GO (Fe_3O_4–NH_2/GO) *via* a simple mixing and chemical cross-linking approach. Amine-functionalized Fe_3O_4 NPs form covalent amide bonds with the carboxylic acid groups on GO.[50]

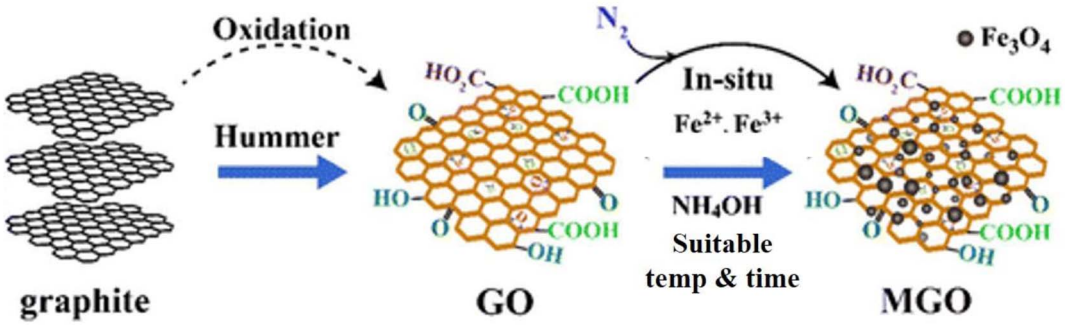

Fig. 3 Schematic illustration of the *in situ* co-precipitation method for preparing magnetic GO (MGO). Graphite is first oxidized to GO *via* a modified Hummers' method, followed by the precipitation of Fe_3O_4 NPs onto the GO surface from Fe^{2+}/Fe^{3+} precursors.[57]

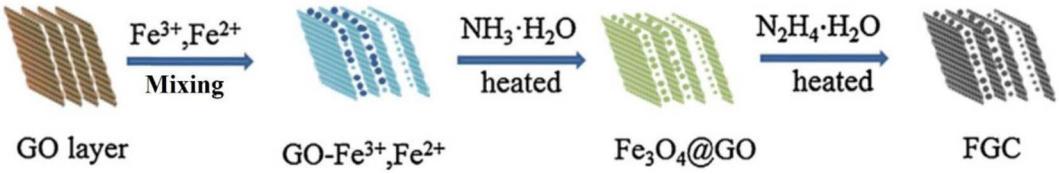

Fig. 4 Schematic diagram of an *in situ* co-precipitation process that includes a chemical reduction step. After the initial formation of Fe_3O_4@GO, a reducing agent ($N_2H_4 \cdot H_2O$) is added to convert GO to rGO, yielding a final composite (FGC).[30]

challenging, potentially leading to inconsistent material performance and underutilization of available surface area.

3.2 Co-precipitation

Co-precipitation is a widely used and highly effective *in situ* method where Fe_3O_4 NPs are nucleated and grown directly on the surface of dispersed graphene derivatives. In a typical procedure, GO is first exfoliated and dispersed in an aqueous solution containing a stoichiometric mixture of Fe^{2+} and Fe^{3+} salts (*e.g.*, $FeCl_2$ and $FeCl_3$), usually in a 1 : 2 molar ratio to favor the formation of Fe_3O_4. The subsequent addition of a base, such as NH_4OH or NaOH, rapidly increases the pH to 10–12. This change in pH induces the simultaneous hydrolysis and co-precipitation of iron ions as Fe_3O_4 NPs directly onto the functionalized GO sheets, which act as nucleation sites.[4,29,33,34,38,40,43,49,52–56] The process is often conducted under an inert atmosphere (*e.g.*, N_2) and at elevated temperatures (*e.g.*, 80–90 °C) to promote the formation of highly crystalline magnetite and prevent oxidation to less magnetic phases, such as maghemite (γ-Fe_2O_3) (Fig. 3).

In some variations, a chemical reducing agent, such as hydrazine hydrate, is introduced after the initial precipitation. This step facilitates the simultaneous reduction of GO to the more conductive rGO, yielding a final Fe_3O_4@rGO composite with potentially different surface properties (Fig. 4).[18,26,30,36] Co-precipitation generally results in a more uniform NP distribution and a stronger, more intimate interaction between the Fe_3O_4 and graphene components compared to simple mixing. However, the method's success hinges on precise control over reaction parameters, such as pH, temperature, stirring rate, and precursor concentration, to avoid uncontrolled NP agglomeration and ensure high batch-to-batch reproducibility.

3.3 Hydrothermal and solvothermal methods

Hydrothermal and solvothermal methods are powerful synthesis techniques that utilize high temperatures (typically

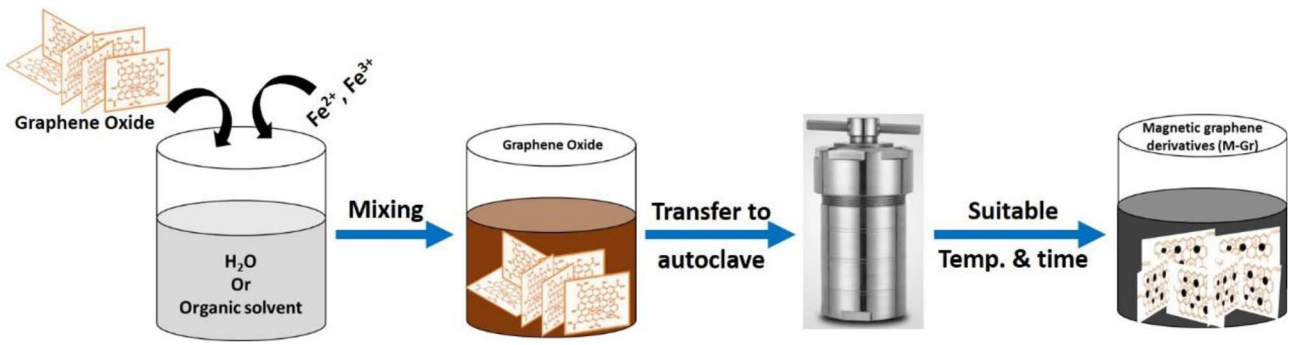

Fig. 5 General schematic of the hydrothermal or solvothermal synthesis process for the synthesis of magnetic graphene derivatives.

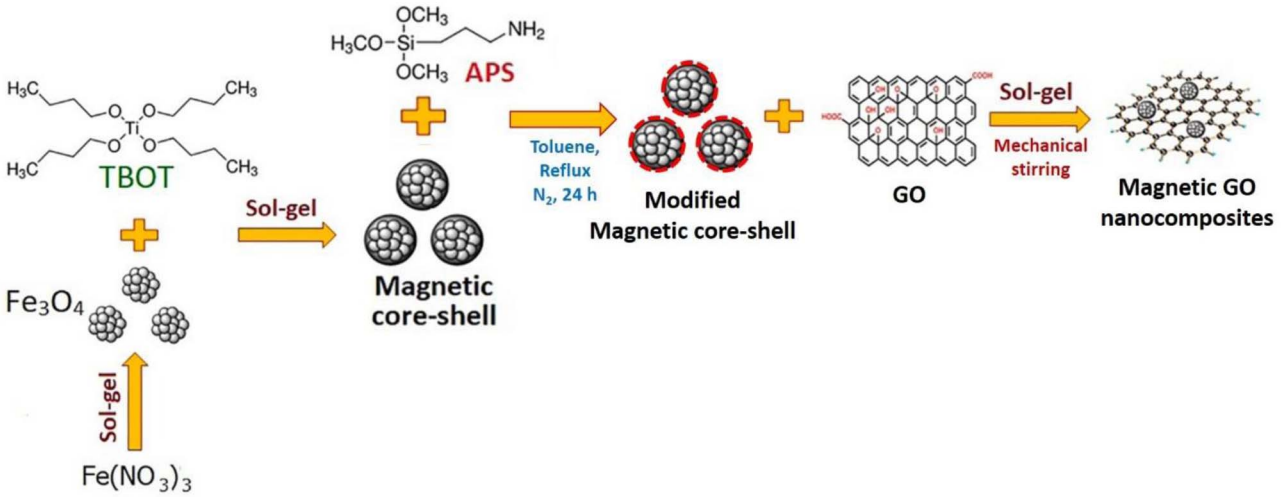

Fig. 6 Schematic of the sol–gel synthesis of a magnetic GO NC. Pre-formed Fe_3O_4 NPs are coated with a silica precursor (TBOT) and functionalized with an amine-containing silane (APS) before being integrated with GO through a sol–gel process.[46]

120–200 °C) and the corresponding autogenous pressures within a sealed vessel (an autoclave) to produce highly crystalline and well-defined NCs (Fig. 5). In this process, GO is dispersed in a solution of iron salt precursors. The distinction lies in the solvent: the hydrothermal method uses water, while the solvothermal method employs an organic solvent with a high boiling point, such as ethylene glycol or diethylene glycol. Under these solvothermal conditions, the iron precursors decompose, and the resulting ions undergo controlled hydrolysis and condensation to nucleate and grow Fe_3O_4 NPs directly on the graphene sheets.[12,13,16,19–21,58]

These methods provide exceptional control over the size, shape (morphology), and crystallinity of the resulting NPs, which, in turn, lead to enhanced, more uniform magnetic

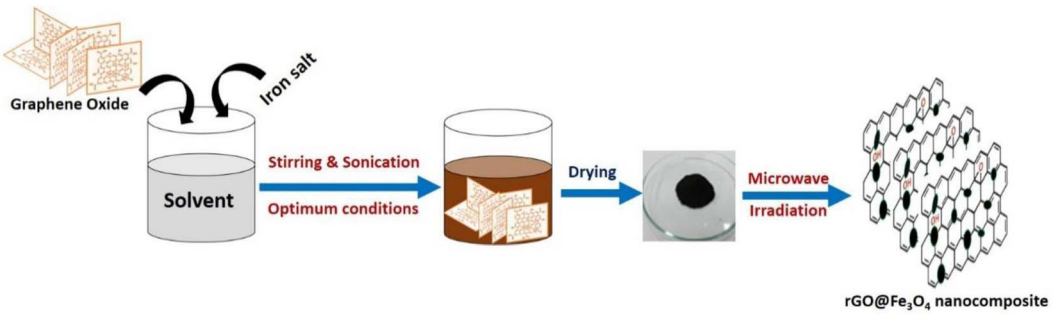

Fig. 7 General schematic of the microwave-assisted synthesis of rGO@Fe_3O_4 NCs. A mixture of GO and iron salt precursors is subjected to microwave irradiation, which simultaneously reduces the GO and forms the Fe_3O_4 NPs.

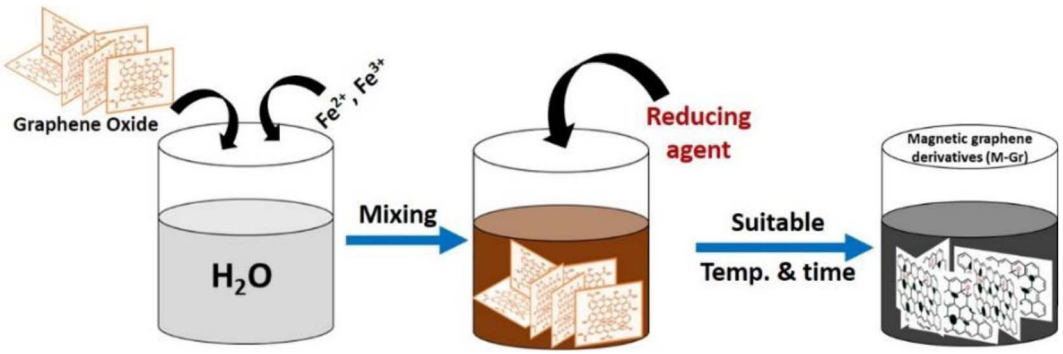

Fig. 8 Schematic diagram of the *in situ* chemical reduction method. A reducing agent is added to a mixture of GO and iron salt precursors, leading to the simultaneous formation of Fe_3O_4 NPs and reduction of GO to rGO.

Table 2 Summary of representative synthesis methods for Fe_3O_4@graphene-based NCs[a]

Composite name	Precursors	Conditions	Ref.
Synthesis method: simple mixing			
PB/Fe_3O_4/GO	GO, Fe_3O_4, $FeCl_3$, $K_4[Fe(CN)_6]$	GO & Fe_3O_4 ultrasonicated in 50 & 300 mL, mixed & stirred 10 min, $FeCl_3$ added, $K_4[Fe(CN)_6]$ added dropwise and stirred 1 h	25
Fe_3O_4–NH_2/GO	$FeCl_3 \cdot 6H_2O$, $FeCl_2 \cdot 4H_2O$, NH_3, APTES, GO, toluene	Fe_3O_4 synthesized at 80 °C for 2 h, dried 60 °C 5 h, APTES functionalization in toluene under N_2 at reflux 24 h, GO dispersed in water + Fe_3O_4–NH_2 (ratios 1 : 1, 1 : 2, 1 : 3), stirred 30 min, NH_4OH added dropwise, stirred 2 h at 80 °C	50
Synthesis method: co-precipitation			
Fe_3O_4/GO	GO, ferric chloride, ferrous chloride	50 °C for 30 min under N_2 by constant mechanical stirring	55
(1) MGO	(1) GO, $FeCl_3 \cdot 6H_2O$ and $FeCl_2 \cdot 4H_2O$	(1) 60 °C for 1 h, stirred under N_2 atmosphere, pH 10	47
(2) MGOC *via* the cross-linking	(2) MGO, chitosan, NaTPP, glutaraldehyde	(2) RT for hydrogel formation, 40 °C drying, 6 h cross-linking at 150 rpm	
Fe_3O_4/GO	GO, $FeCl_3 \cdot 6H_2O$, $FeCl_2 \cdot 4H_2O$, NH_3	90 °C for 8 h under N_2, pH adjusted to 10.5	4
Magnetic GO	GO, $FeCl_3 \cdot 6H_2O$, $FeSO_4 \cdot 7H_2O$, NH_4OH	pH 10, RT, 4 h, N_2 atmosphere	54
M-GO	GO, $FeCl_3 \cdot 6H_2O$, $FeCl_2 \cdot 4H_2O$, NH_3	Ultrasonicated at 85 °C, pH 10, 30 min sonication	33
M-GO	GO, $FeCl_3 \cdot 6H_2O$, $FeCl_2 \cdot 4H_2O$, NH_3	Alkaline pH	29
MGO	GO, $(NH_4)_2Fe(SO_4)_2 \cdot 6H_2O$, $FeCl_3 \cdot 6H_2O$, NH_3, HCl	80 °C under N_2, stirred 1 h	34
(1) MGOs	(1) GO, $FeCl_3 \cdot 6H_2O$, $FeCl_2 \cdot 4H_2O$, H_2O_2	(1) 90 °C for 8.5 h under N_2, dried at 60 °C for 24 h	1
(2) CMC/MGOs *via* plasma-induced grafting	(2) MGOs, carboxymethyl cellulose (CMC), N_2 gas	(2) Plasma activation: 45 min (10 Pa, 950 V, 120 W); grafting: 60 °C, 48 h	
SMGO	Disaccharide sugar, O_3, $FeCl_3 \cdot 6H_2O$, $FeCl_2 \cdot 4H_2O$, NaOH	80 °C for 1 h, pH ≥ 10, under N_2 atmosphere	38
MCGO	GO, $FeCl_3 \cdot 6H_2O$, $FeCl_2 \cdot 4H_2O$, NH_3, HCl, acetic acid	Sonication + 12 h stirring, pH adjusted to 8 under N_2	40
GO/Fe_3O_4/GC	GO, graphitic carbon (GC), $FeSO_4 \cdot 7H_2O$, $NH_3 \cdot H_2O$	Ultrasonicated 3 h, pH 11, stirred 3 h	49
M/GO	GO, $FeCl_3 \cdot 6H_2O$, $FeCl_2 \cdot 4H_2O$, NH_3	85 °C, pH 10, stirred 45 min	52
Fe_3O_4/GO	GO, $FeCl_3 \cdot 6H_2O$, $FeCl_2 \cdot 4H_2O$, NH_3	Room temp to 80 °C, pH 10; 45 min stirring	56
MGO	GO, $FeCl_3 \cdot 6H_2O$, $FeCl_2 \cdot 4H_2O$, $NH_3 \cdot H_2O$	pH pre-adjusted, stirred for 3 h at 80 °C	57
MGO	GO, $FeCl_3$, $FeCl_2$, NH_4OH, hydrazine hydrate	80 °C, under N_2, stirred	18
(1) MGO	(1) GO, $FeCl_3$, $FeCl_2$, NH_4OH, hydrazine hydrate	(1) 80 °C under N_2, stirred	26
(2) PBMGO	(2) GO, Fe_3O_4, $FeCl_3$, $K_4[Fe(CN)_6]$	(2) Room temp; stirred 1 h	
FGC	GO, $FeCl_3 \cdot 6H_2O$, $FeCl_2 \cdot 4H_2O$, NH_4OH, hydrazine hydrate	pH 10, 80 °C, stirred for 5 h	30
Fe_3O_4/rGO	GO, $FeCl_3$, $FeCl_2$, NH_4OH, hydrazine hydrate	80 °C, stirred for 5 h	35
Synthesis method: hydrothermal			
Magnetic PANI/GO	GO, aniline, $(NH_4)_2S_2O_8$, $FeCl_3$, $FeCl_2$, NH_3, hydrazine hydrate	90 °C, stirred for 4 h under N_2, pH 10	17
FGC	GO, $FeCl_3$, $FeCl_2$, 30% ammonia solution	180 °C for 10 h	12
Fe_3O_4/rGO	GO, $FeCl_3 \cdot 6H_2O$, sodium acetate, aqueous ammonia, diethylene glycol	180 °C for 12 h in autoclave	16
GN–Fe_3O_4	GO, $FeCl_3 \cdot 6H_2O$, ascorbic acid, hydrazine hydrate	180 °C, 8 h (autoclave), then 500 °C calcination (4 h, N_2)	58
Synthesis method: solvothermal			
MGONRs	GONRs, $FeCl_3 \cdot 6H_2O$, sodium acetate, ethylene glycol	200 °C for 6 h, vacuum drying at 60 °C for 12 h	13
Fe_3O_4/GO	GO, ethylene glycol, $FeCl_3 \cdot 6H_2O$, NaAc	190 °C for 6 h, vacuum oven at 60 °C for 24 h	20
EDTA–mGO	(1) GO, ethylene glycol, NaAc, $FeCl_3 \cdot 6H_2O$ (2) mGO, HAC, ethylene glycol, EDTA	(1) 190 °C for 6 h (2) Stirred for 4 h at 60 °C, dried in a vacuum oven at 60 °C for 24 h	21
UiO-66/Fe_3O_4/GO	GO, Fe_3O_4, $ZrCl_4$, PTA, DMF	120 °C for 24 h in autoclave; sonication + stirring pre-treatment	19

Table 2 (*Contd.*)

Composite name	Precursors	Conditions	Ref.
Synthesis method: sol–gel method			
TBOT–GO–Fe_3O_4	GO, $Fe(NO_3)_3 \cdot 9H_2O$, ethylene glycol, TBOT, 3-aminopropyltrimethoxysilane, ammonia, nitric acid, ethanol, water, toluene	100 °C, 6 h reflux, surface modification: reflux 24 h under N_2 atmosphere, final drying at 80 °C	46
Fe_3O_4/graphene	Potassium humate, $FeCl_3 \cdot 6H_2O$, NaCl	Stir at 70 °C for 12 h, dry at 70 °C for 48 h, mix with NaCl, calcine at 500/600/700 °C for 4 h under Ar (10 °C min^{-1})	59
Synthesis method: microwave-assisted synthesis			
SPION–rGO	GO, $Fe(acac)_3$, benzyl alcohol	Disperse GO in benzyl alcohol, mix with $Fe(acac)_3$, microwave heating in 2-stage program	39
Fe_3O_4@SiO_2–GO	Fe_3O_4@SiO_2, 3-aminopropyltriethoxysilane, GO, NHS, EDC, isopropanol	Functionalize Fe_3O_4@SiO_2 with silane, react with GO–EDC/NHS at 60 °C, 80 W for 4 h	48
rGO@Fe_3O_4	Graphite oxide, EtOH, $FeCl_3 \cdot 6H_2O$, diluted $NH_3 \cdot H_2O$	Magnetic stirring, sonication, addition of Fe salt & $NH_3 \cdot H_2O$, drying at 50 °C, microwave irradiation (900 W, 45 s)	61
Synthesis method: *in situ* chemical reduction			
Fe_3O_4/rGO	GO, $FeCl_3$, $FeCl_2$, $NH_3 \cdot H_2O$, hydrazine hydrate	$FeCl_3$ and $FeCl_2$ added slowly to GO, NH_3 added to precipitate Fe_3O_4, stirred 5 h at 80 °C	35
Fe_3O_4/RGO	GO, $FeCl_3 \cdot 6H_2O$, *Murraya koenigii* leaf extract	Stirred 1 h, refluxed 5 h at 80 °C	42
rGO/Fe_3O_4	GO, $FeSO_4 \cdot 7H_2O$, $FeCl_3 \cdot 6H_2O$, *Dolichos lablab* pod extract	Sonicated 1 h, extract added & stirred 1 h at 30 °C, NH_3 adjusted pH10, heated 80 °C for 12 h	62

[a] PB, Prussian blue; PANI, polyaniline; NaTPP, sodium tripolyphosphate; APTES, 3-aminopropyltriethoxysilane; TBOT, tetrabutyl orthotitanate; DMF, dimethylformamide.

properties and a robust, stable interface between the two components. The high-temperature environment can also facilitate the partial reduction of GO to rGO. The primary drawbacks of these techniques are the need for specialized, costly high-pressure equipment, significantly longer reaction times (often several hours to a full day), and higher energy consumption, which can be limiting factors for large-scale industrial production.

3.4 Other synthesis methods

Several other advanced techniques have been successfully applied to the synthesis of Fe_3O_4@graphene NCs, each offering unique advantages and challenges.

The sol–gel method is a versatile bottom-up approach that involves transforming a liquid colloidal suspension ("sol") into a solid three-dimensional network ("gel"). In this context, molecular precursors (*e.g.*, iron alkoxides) undergo hydrolysis and polycondensation in a sol containing a dispersed carbon source, such as GO. This process results in a gel where Fe_3O_4 NPs are homogeneously embedded within the interconnected graphene matrix. Subsequent aging, drying, and thermal treatment (calcination) yield the final porous composite (Fig. 6).[46,59] This method offers exquisite control over the material's final composition and porosity, but is often a multi-step, complex process that can be prone to structural defects, such as cracking, during solvent removal.

Microwave-assisted synthesis represents a significant intensification strategy for process development. It uses microwave radiation to deliver energy directly and efficiently to the polar molecules in the reaction mixture, resulting in rapid, uniform heating. This dramatically reduces reaction times (often from hours to minutes) and lowers overall energy consumption compared to conventional heating methods (Fig. 7). The technique promotes the rapid nucleation and controlled growth of Fe_3O_4 NPs on the graphene surface, offering excellent control over particle size and distribution.[39,48,60,61] However, it requires specialized microwave reactor equipment, and the limited penetration depth of microwaves can pose a challenge for scaling up to large reaction volumes.

In situ chemical reduction is an elegant one-pot approach that simultaneously reduces GO to rGO and forms Fe_3O_4 NPs from their salt precursors. This is achieved by introducing a chemical reducing agent, which can range from conventional reagents, such as sodium borohydride or hydrazine hydrate, to more environmentally friendly "green" reagents like plant extracts, into the reaction mixture (Fig. 8).[35,42,62]

This method is highly efficient and promotes the formation of strong chemical bonds between the components. The main challenge lies in carefully controlling the reduction kinetics to prevent the uncontrolled, rapid growth and subsequent agglomeration of the NPs.

A summary of various synthesis approaches and their corresponding conditions is provided in Table 2. A schematic overview of these methods is presented in Fig. 9.

4.0 Characterization of Fe_3O_4@graphene NCs

A comprehensive and multifaceted characterization of Fe_3O_4@graphene NCs is essential to fundamentally understand

their structure–property relationships, which, in turn, enables the optimization of their performance in targeted applications. A suite of complementary analytical techniques is typically employed to probe their crystallographic, morphological, chemical, and magnetic properties in detail.

4.1 Crystallographic analysis: X-ray diffraction (XRD)

XRD is a fundamental and indispensable technique for identifying crystalline phases in a material and determining key structural properties. For Fe_3O_4@graphene NCs, XRD patterns consistently confirm the successful formation of the desired iron oxide phase. They typically exhibit a set of characteristic diffraction peaks at 2θ values of approximately 30.1°, 35.4°, 43.1°, 57.0°, and 62.5°. These peaks can be indexed to the (220), (311), (400), (511), and (440) crystallographic planes, respectively, which is the definitive fingerprint of the inverse spinel crystal structure of magnetite (Fe_3O_4) (JCPDS file no. 19-0629).[30,33,41] Interestingly, the characteristic broad diffraction peak of GO, which arises from the regular stacking of oxidized sheets and is typically observed around $2\theta = 10–11°$, is often significantly diminished, broadened, or even completely absent in the final composite's XRD pattern (Fig. 10). The observation is highly informative, indicating that the integration of Fe_3O_4 NPs has effectively disrupted the regular layer-by-layer stacking of GO sheets, leading to a more exfoliated and disordered

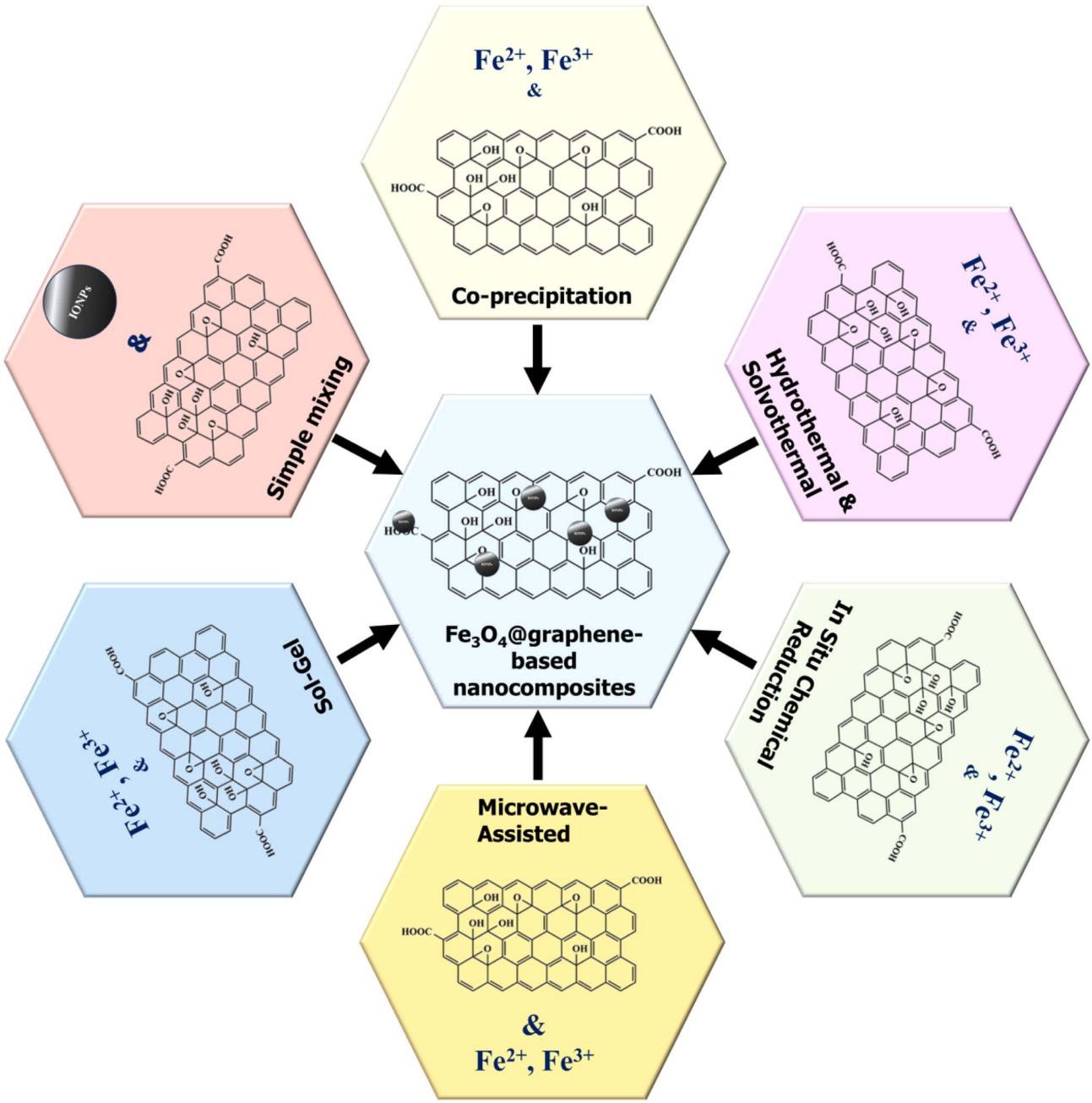

Fig. 9 Schematic overview of the primary synthesis methods for producing Fe_3O_4@graphene-based NCs.

structure.[12,18] In composites where GO is deliberately reduced to rGO, a new broad peak corresponding to the restacked rGO sheets may appear at a higher angle, around $2\theta = 24°$.[35] Furthermore, the width of the Fe_3O_4 diffraction peaks can be used in conjunction with the Scherrer equation to provide a reliable estimate of the average crystallite size, which typically falls within the desired nanometer range.[30,41] A summary of XRD findings from a range of studies is presented in Table 3.

4.2 Morphological and microstructural analysis: electron microscopy (SEM and TEM)

Scanning Electron Microscopy (SEM) and Transmission Electron Microscopy (TEM) are indispensable tools for visualizing the morphology, particle size, and spatial distribution of the components within the NC. SEM provides detailed information about the surface topography, revealing how the Fe_3O_4 NPs are distributed across the larger, often wrinkled, sheet-like structure of the graphene matrix (Fig. 11). An ideal morphology, typically sought after, is a uniform, dense NP decoration, as this configuration is most effective at preventing graphene sheet restacking, thereby maximizing the accessible surface area for sorption.[12,20,61]

TEM offers significantly higher resolution, enabling the detailed analysis of individual NP size and shape, as well as a clear visualization of their interface with the graphene support. TEM images characteristically show the translucent, veil-like sheets of graphene decorated with dark, electron-dense Fe_3O_4 NPs (Fig. 12). At very high magnifications, High-Resolution TEM (HRTEM) can even resolve the lattice fringes of the individual crystalline Fe_3O_4 NPs, providing direct visual confirmation of their high crystallinity and structural integrity.[41] Collectively, these powerful microscopy techniques confirm the synergistic architecture of the composite: the graphene sheets act as a high-surface-area support that prevents the magnetic NPs from agglomerating, while the NPs, in turn, act as spacers that prevent the graphene sheets from collapsing and restacking. This mutual stabilization is a key factor in the material's high performance. Table 4 summarizes morphological observations from various representative studies.

4.3 Surface and textural properties: BET surface area analysis

The Brunauer–Emmett–Teller (BET) method, based on the physical sorption of nitrogen gas at cryogenic temperatures, is the standard technique for quantifying the specific surface area and pore characteristics of porous materials. These parameters are of paramount importance for sorption applications, as they directly relate to the number of available binding sites. As detailed in Table 5, the specific surface areas of these NCs can vary dramatically, from as low as ~40 $m^2 g^{-1}$ to well over 400 $m^2 g^{-1}$, with this variation directly determined by the chosen synthesis conditions and the resulting material architecture.[12,38] The analysis also yields critical information on the total pore volume and the average pore diameter. The data often reveal a predominantly mesoporous structure (pores between 2 and 50 nm), which is considered ideal for environmental remediation applications because it allows unhindered diffusion of hydrated ions from the bulk solution to the internal sorption sites.[12,21,61] For example, Zhao *et al.*[12] reported a BET surface area of 42.53 $m^2 g^{-1}$ and an average pore diameter of 15.71 nm for their magnetic composite, confirming its mesoporous nature. In stark contrast, a composite synthesized by Pu *et al.*[57] under different conditions exhibited a much higher surface area of 407 $m^2 g^{-1}$, highlighting the tunability of these materials. These textural properties are crucial inputs for accurately modeling and predicting the material's ultimate sorption capacity.

4.4 Chemical and functional group analysis: FTIR and Raman spectroscopy

Fourier Transform Infrared (FTIR) spectroscopy is a powerful technique for identifying the chemical functional groups present on the surface of the NC and for confirming the successful integration of the constituent components. The FTIR

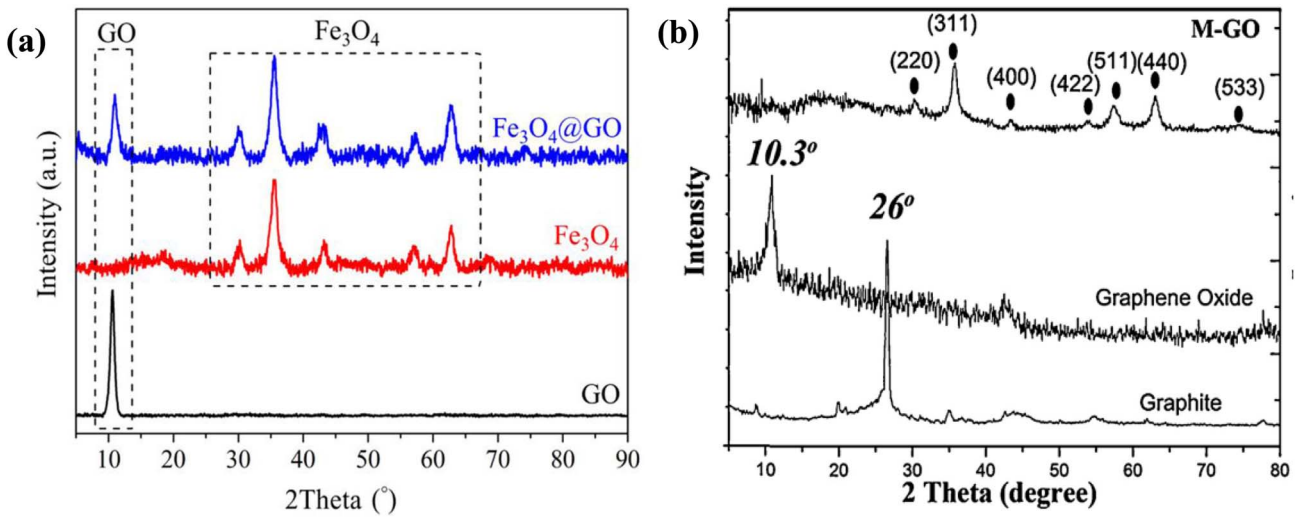

Fig. 10 Representative XRD patterns of (a) graphite, GO, and a magnetic GO (M-GO) composite, and (b) a different M-GO hybrid, demonstrating the characteristic peaks of the Fe_3O_4 phase and the change in the GO peak upon composite formation.[33,41]

spectrum of a typical Fe_3O_4@graphene composite displays the characteristic absorption bands associated with GO, including a broad peak for hydroxyl (–OH) stretching vibrations around 3400 cm^{-1}, a sharp peak for carboxyl (C=O) stretching at ~1730 cm^{-1}, vibrations from aromatic (C=C) bonds at ~1620 cm^{-1}, and absorptions from epoxy (C–O) groups at ~1220 cm^{-1}. A definitive indicator of successful composite formation is the appearance of a new, strong absorption band in the low-wavenumber region, typically around 580 cm^{-1}, which is the characteristic vibrational mode of the Fe–O bond within the Fe_3O_4 crystal lattice (Fig. 13). Furthermore, a noticeable reduction in the intensity of the peaks corresponding to oxygen-containing functional groups in the composite, when compared to the spectrum of pure GO, can provide evidence of both chemical interaction with the Fe_3O_4 NPs and the partial reduction of GO during the synthesis process.[12,13] A summary of key FTIR peaks reported in the literature is provided in Table 6.

Raman spectroscopy is an exceptionally sensitive tool for probing the structural integrity, electronic properties, and degree of disorder within the carbon lattice of the graphene component. The Raman spectrum of graphene-based materials is characteristically dominated by two prominent peaks: the D band (at ~1350 cm^{-1}), which is activated by structural defects, edges, and sp^3-hybridized carbon atoms, and the G band (at ~1580 cm^{-1}), which arises from the in-plane vibrational mode of the sp^2-hybridized carbon atoms that form the graphitic lattice. The intensity ratio of these two bands (I_D/I_G) is a widely accepted metric for quantifying the level of defects and disorder in the graphene structure. An increase in the I_D/I_G ratio in the composite relative to the starting GO is often observed, which can be interpreted as the formation of new, smaller graphitic

Table 3 Summary of XRD data for various Fe_3O_4@graphene-based NCs

No.	Composite name	2θ (°) values	Planes (*hkl*)	Crystal nature	Crystallite size (nm)	Particle size (nm)	Ref.
1	Fe_3O_4@graphene	10.3 (GO), 18.27, 30.1, 35.4, 43.05, 56.94, 62.51, and 73.95	(001) GO, (111), (220), (311), (400), (422), (511), (553)	Inverse spinel		~32	30
2	Fe_3O_4@GO	11.0 (GO), 30.1, 35.5, 43.1, 57.0, and 62.7	(002) GO, (220), (311), (400), (511), and (440)		8–9		41
3	Fe_3O_4/RGO (9 : 1)	23.9 (RGO), 18.7, 30.1, 35.5, 43.2, 54.1, 57.3, and 62.9	(002) RGO, (111), (220), (311), (400), (422), (511), and (440)	Cubic		~30	35
4	M-GO	30.1, 35.4, 37.1, 43.1, 53.4, 56.9, and 62.5	(220), (311), (222), (400), (422), (511), and (440)				33
5	Magnetic Fe_3O_4/graphene	29.8, 35.2, 43.1, 53.9, 57.2, and 62.9	(220), (311), (400), (422), (511), (440)				12
6	MGO	30.2, 35.6, 43.3, 53.7, 57.1, and 62.8		Cubic spinel	11.2 ± 8		18
7	EDTA–mGO	34.3, 43.2, 53.3, 57.5, and 63.2	(220), (311), (400), (422), (551), and (440)				21
8	RGO/Fe_3O_4	30.2, 35.5, 43.2, 53.5, and 62.6	(220), (311), (400), (422) and (440)	Face-centred cubic			42
9	MGO/chitosan	20.8 (chitosan), 30.1, 35.4, 43.2, 53.6, 57.1, and 62.6	(220), (311), (400), (422), (511), and (440)	Face-centred cubic			47
10	SMGO	30.0, 35.4, 43.1, 53.6, 57.2, and 62.7	(220), (311), (400), (422), (511), and (440)	Cubic	12.1		38
11	Fe_3O_4/GO	30.23, 35.21, 43.15, 53.43, 57.22, and 62.52	(220), (311), (400), (422), (511), and (440)	Face-centred cubic			20
12	PB/Fe_3O_4/GO	30.2, 35.6, 43.3, 53.7, 57.3, 62.8, 74.9, 17.4 (PB), 24.8 (PB), 35.3 (PB), and 39.5 (PB)	(220), (311), (400), (422), (511), (440), and (533)	Cubic spinel			31
13	Fe_3O_4–NH_2/GO (3 : 1)	18.1, 30.0, 35.4, 43.3, 53.4, 57.1, and 62.7	(111), (220), (311), (400), (422), (511), and (440)	Inverse-spinel	12.13		50
14	(mGOi)	18.27°, 30.1°, 35.4°, 43.05°, 56.94°, 62.51°, and 73.95°	(111), (220), (311), (400), (422), (511), and (553)	Spinel	18.4		56
15	Fe_3O_4–GO	26.5, 30.42, 35.06, 43.48, 53.22, 57.78, and 63.06		Cubic spinal			43
16	FeNPs/rGO	26 (rGO), 44 (Fe_3O_4)				80–85	63
17	Fe_3O_4@SiO_2@GO	18.31, 30.12, 35.39, 43.06, 54.93, 57.53, 63.45, and 73.92	(111), (220), (311), (400), (422), (511), (440), and (553)				48
18	rGO/Fe_3O_4	21 (GO), 33.09, 35.64, 43.44, 53.91, 57.41, and 62.9	(002) rGO, (220), (311), (400), (422), (511), and (440)	Face-centred cubic	38		64

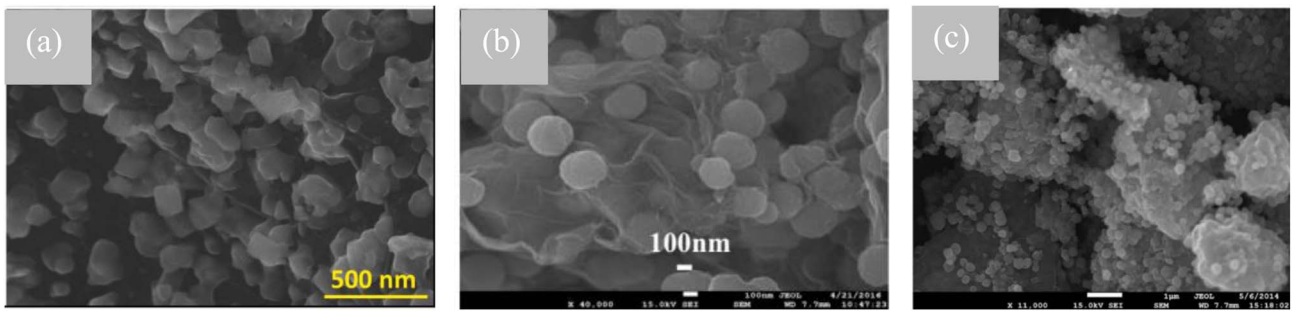

Fig. 11 Representative SEM images of various magnetic graphene composites (a) rGO@Fe_3O_4, (b) Fe_3O_4/graphene, and (c) Fe_3O_4/GO, showing Fe_3O_4 NPs distributed on the surface of graphene sheets.[12,20,61]

domains or an increase in defect sites during chemical processing and NP integration.[12] Conversely, a decrease in this ratio may indicate a specific chemical interaction between the NPs and the existing defect sites on the GO surface, which can restrict the vibrational freedom of those atoms.[33] The Raman spectrum of the composite may also exhibit characteristic vibrational modes of Fe_3O_4 (*e.g.*, a peak around 670 cm^{-1}), providing further confirmation of its presence (Fig. 14). Table 7 summarizes Raman spectral data from various studies.

4.5 Compositional and stability analysis: XPS and TGA

X-ray photoelectron spectroscopy (XPS) is a surface-sensitive analytical technique that provides quantitative information about the elemental composition and, crucially, the chemical (oxidation) states of the atoms on the material's surface. A survey scan of the composite readily confirms the presence of the expected elements: C, O, and Fe. High-resolution scans of specific elemental regions provide deeper insight. The C 1s region can be deconvoluted into multiple peaks corresponding to different carbon–oxygen functional groups (*e.g.*, C–O, C═O, O–C═O), enabling a quantitative assessment of surface chemistry. The Fe 2p spectrum, with its characteristic Fe $2p_{3/2}$ and Fe $2p_{1/2}$ spin–orbit split peaks (located at binding energies of ~711 eV and ~724 eV, respectively), confirms the presence of iron in a mixed +2 and +3 oxidation state, which is consistent with the Fe_3O_4 stoichiometry.[25,31,33,52,58] Most importantly, a careful analysis of the O 1s spectrum can often reveal a distinct chemical environment associated with the formation of Fe–O–C bonds. This provides direct spectroscopic evidence of a covalent linkage between the iron oxide NPs and the graphene support, which is essential for the long-term stability and integrity of the composite (Fig. 15).[33] Table 8 summarizes key XPS findings from the literature.

Thermogravimetric Analysis (TGA) is used to assess the thermal stability of the NCs and to determine their approximate composition. The TGA curve plots the percentage weight loss of a sample as it is heated at a controlled rate. A typical TGA curve for a Fe_3O_4@-graphene composite shows several distinct weight-loss stages. An initial weight loss below ~150 °C is attributed to the desorption of physically adsorbed water. This is followed by a more significant weight loss, typically occurring between ~200 °C and 500 °C, which corresponds to the thermal decomposition of the labile oxygen-containing functional groups and, at higher temperatures, the combustion of the carbon skeleton of the graphene component. The mass that remains at the end of the analysis at high temperatures corresponds to the thermally stable inorganic component, Fe_3O_4 (which may be oxidized to Fe_2O_3 if the study is conducted in an air atmosphere). By comparing the total weight loss to that of pure GO under the same conditions, the relative mass percentage of Fe_3O_4 in the composite can be reliably estimated. These analyses generally show that the composites exhibit significantly enhanced thermal stability compared to pure GO, a result of the protective and stabilizing effects of the integrated iron oxide NPs.[1,12,36,49] Table 9 summarizes TGA results from various studies.

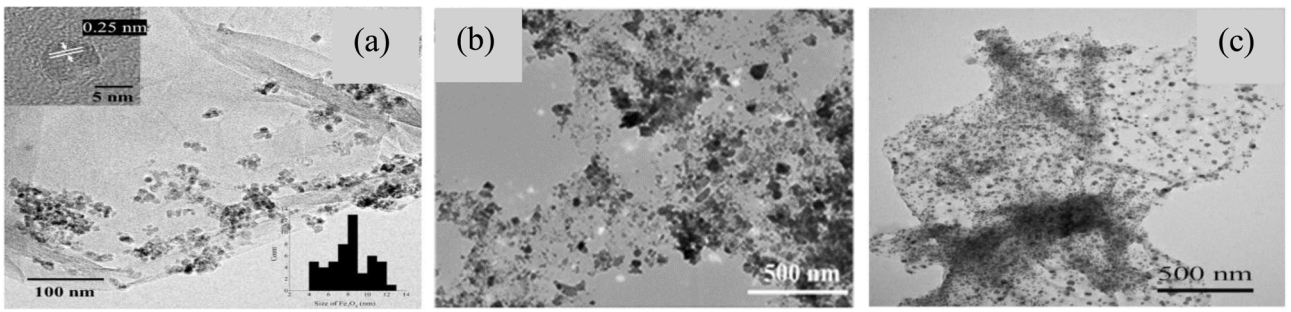

Fig. 12 Representative TEM images of magnetic graphene composites (a) Fe_3O_4@GO, (b) Fe_3O_4/GO, and (c) Fe_3O_4/rGO, providing a higher-resolution view of the uniform dispersion of Fe_3O_4 NPs on the translucent graphene sheets. The inset in (a) is an HRTEM image showing the crystalline lattice of an Fe_3O_4 NP.[41,55,65]

Table 4 Summary of morphological characteristics of Fe_3O_4@graphene-based NCs observed *via* SEM and TEM[a]

No.	Composite name	Technique	Observed morphology	Particle size/layer thickness	Ref.
1	Fe_3O_4/GO	TEM	Fe_3O_4 NPs are uniformly and homogeneously decorated on GO flakes		55
2	MGO/chitosan	SEM	Fe_3O_4 particles are anchored on a much rougher surface than the GO surface		47
3	SMGO	TEM	Small Fe_3O_4 particles are dispersed on a transparent and thin carbon sheet	16 nm	38
4	GO/Fe_3O_4	SEM	Fe_3O_4 particles are embedded on GO sheets		20
5	Fe_3O_4/graphene	SEM & TEM	Fe_3O_4 MNPs are dispersed on the surface of graphene homogeneously	340 nm	12
6	PB/Fe_3O_4/GO	TEM	PB coating Fe_3O_4 NPs inhomogeneously anchored on the surface of the GO sheets	15 nm	31
7	UiO-66/Fe_3O_4/GO	SEM & TEM	UiO-66/Fe_3O_4 NPs are disorderly dispersed in the wrinkles of the GO sheet		19
8	PMMA/GO–Fe_3O_4	SEM	Fe_3O_4 particles are embedded in PMMA/GO		53
9	Fe_3O_4–NH_2/GO (2 : 1)	SEM	Fe_3O_4 NPs loaded on GO sheets	25 nm	50
10	Fe_3O_4@GO	TEM	Fe_3O_4 NPs uniformly dispersed in GO sheets	8.9 ± 0.9 nm	41
11	Fe_3O_4@SiO_2@ GO	TEM	GO forms the outermost shell layer on the SiO_2-coated	500 nm	48
12	(GO)/Fe_3O_4	TEM	Elliptical and circular Fe_3O_4 NPs were uniformly dispersed on the translucent GO	9.8 nm	57
13	rGO@Fe_3O_4	SEM	rGO nanosheets fully loaded with faceted-like Fe_3O_4 NPs	100–150 nm	61
14	rGO/Fe_3O_4	SEM & TEM	The Fe_3O_4 NPs were homogeneously assembled on the surface of RGO sheets	12 nm	42
15	Graphene–Fe_3O_4	TEM	Two-dimensional graphene sheets densely decorated with spherical Fe_3O_4 NPs	7 nm	58
16	rGO/Fe_3O_4	FESEM	Spherical Fe_3O_4 NPs are uniformly anchored on randomly dispersed rGO.	9.75 to 14.85 nm	62
17	rGO/Fe_3O_4	FESEM	Crumpled rGO sheets with closely packed quasi-spherical Fe_3O_4 NPs covering the surface	<10 nm	16
18	PB/Fe_3O_4/GO	SEM & TEM	PB/Fe_3O_4 NPs inhomogeneously anchored on GO sheets	17 nm	25

[a] PB, Prussian blue; PMMA, polymethyl methacrylate.

4.6 Magnetic properties: vibrating sample magnetometry (VSM)

VSM is the standard and most direct technique for characterizing the bulk magnetic properties of the NCs. The instrument measures the sample's magnetic moment as a function of an applied external magnetic field, generating a magnetic hysteresis loop. For well-synthesized Fe_3O_4@graphene NCs, these plots typically exhibit a characteristic "S" shape, with negligible coercivity (the field required to return the magnetization to zero) and remanence (the residual magnetization at zero field). It is the definitive signature of super-paramagnetic behavior. This result is critical, as it confirms that the material is strongly magnetic only when a field is applied and does not retain any permanent magnetism when the field is removed. This property is crucial for preventing magnetic aggregation and facilitating the easy redispersion of the sorbent in solution for reuse.

The saturation magnetization (M_s), which represents the maximum achievable magnetization and is measured from the hysteresis loop plateau, is a key performance parameter. As shown in Table 10, the M_s values for these composites typically range from approximately 10 to over 60 emu g^{-1}.[4,28,43,50,52,58] As expected, this value is lower than that of bulk Fe_3O_4 due to the presence of the non-magnetic graphene component. However, it is more than sufficient for rapid, effective magnetic separation from an aqueous solution using a conventional permanent magnet.

5.0 Application in radionuclide sorption

The unique constellation of properties inherent to Fe_3O_4@-graphene NCs—namely, high surface area, abundant and tunable surface functional groups, and rapid magnetic separability—makes them exceptionally effective sorbents for the challenging task of removing radioactive ions from contaminated water. These materials offer significant performance advantages over many traditional remediation technologies.

Table 5 Summary of textural properties of various Fe_3O_4@graphene-based NCs determined by BET analysis

No.	Composite name	BET surface area ($m^2\ g^{-1}$)	Pore volume ($cm^3\ g^{-1}$)	Average pore diameter (nm)	Pore structure	Ref.
1	MGO/chitosan	169.7				47
2	SMGO	428	0.146			38
3	Magnetic–PANI/GO	86.53				17
4	EDTA–mGO	54.32		16.5	Mesoporous	21
5	Fe_3O_4/graphene	42.53	0.26	15.71	Mesoporous	12
6	UiO-66/Fe_3O_4/GO	171.79	0.11162	8.9332		19
7	GO–Fe_3O_4	124.37		0.386		43
8	rGO@Fe_3O_4	241	0.39	6.4	Mesoporous	66
9	GO/Fe_3O_4	407.1267				57
10	rGO@Fe_3O_4	113	0.0068	4–20	Mesoporous	61
11	M/GO	126				60
12	RGO/Fe_3O_4	58				42
13	GN–Fe_3O_4	221	0.299		Mesoporous	58
14	M2–Fe_3O_4/RGO	326	0.303			65
15	3D MPBRGO	402.62		4.34	Mesoporous	45
16	PB/Fe_3O_4/GO	152.91				25
17	MNGO	124.37		0.386		67

5.1 Sorption performance for key radionuclides

A substantial body of research has demonstrated the high sorption capacity of these NCs for a range of environmentally and radiologically significant radionuclides, including uranium (as the uranyl cation, U(VI)), cesium (Cs(I)), strontium (Sr(II)), and thorium (Th(IV)). As summarized in the comprehensive Table 11, the maximum sorption capacities (q_{max}) reported in the literature are often substantial and highly competitive. For example, a functionalized $FeWO_4$/GO composite has shown an exceptional capacity for U(VI) removal, reaching an impressive 625 mg g^{-1}.[28] Similarly, a novel magnetic Prussian blue/GO aerogel, which combines the ion-sieving properties of Prussian blue with the magnetic graphene scaffold, exhibited a remarkable capacity of 484.12 mg g^{-1} for the selective capture of Cs(I).[45]

Kinetic studies consistently show that the sorption process is well-described by the pseudo-second-order kinetic model. It indicates that the rate-limiting step is chemisorption, which involves valence forces through the sharing or exchange of electrons between the sorbent and the radionuclide. Furthermore, the equilibrium data often exhibit an excellent fit to the Langmuir isotherm model, which assumes monolayer sorption onto a finite number of identical, homogeneous active sites. Collectively, these findings underscore the immense potential of these materials for the efficient and high-capacity sequestration of hazardous radioactive contaminants from aqueous solutions.

5.2 Underlying sorption mechanisms

The efficient removal of radionuclides by Fe_3O_4@graphene NCs is not the result of a single process but rather a complex interplay of multiple physical and chemical interaction mechanisms, as illustrated schematically in Fig. 16. A thorough and nuanced understanding of these mechanisms is crucial for the

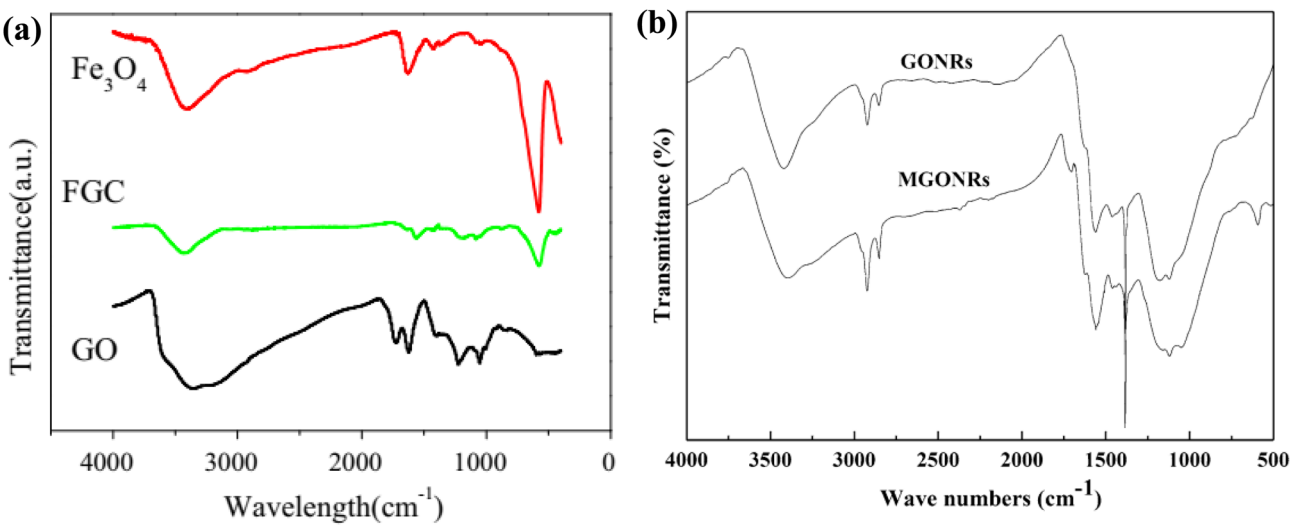

Fig. 13 Representative FTIR spectra of (a) GO and a magnetic composite (FGC), and (b) GO nanoribbons (GONRs) and their magnetic composite (MGONRs). The appearance of a peak around 580 cm^{-1} in the composites confirms the presence of Fe–O bonds from Fe_3O_4.[12,13]

Table 6 Summary of characteristic functional groups in Fe_3O_4@graphene-based NCs identified by FTIR spectroscopy

No.	Composite name	Prominent FTIR peaks (cm^{-1})	Designated functional groups	Observed shifts	Ref.
1	RGO/Fe_3O_4	3328, 2952, 1658, 1449, 1122, and 585	–OH, C–H (methyl), C═O, C═C, C–OH, and Fe–O	O–H band shifted, weakened, new Fe–O peak at 585	42
2	MGO/chitosan	3400, 2750–3600, 1724, 1660, 1620, 1402, 1377, 1068, 1053, and 580	O–H, –NH/–OH (broad), C═O (COOH), amide (–NHCO), C═C/ C–OH/O–H bending, C–H (–CH_3), C–O–C, and Fe–O (Fe_3O_4)	Slight intensity changes in 1660, 1377, and 1068 peaks; Fe–O peak at 580 retained	47
3	MGONRs	3440, 2920, 2850, 1731, 1558, 1397, 1095, and 586	–OH, –CH (symmetric & asymmetric), C═O, C–C (graphite), C–O, and Fe–O	Fe–O peak at 586 cm^{-1} appears in MGONRs	13
4	mGO–PP	592, 2931, 2849, 2245, 1656, and 941	Fe–O, CH_2, CH (PEI), C≡N (PAN), C═N, and N–O	Disappearance of C≡N (2245 cm^{-1}); new peaks C═N and N–O after hydroxylamine treatment	68
5	Fe_3O_4/GO	3420, 1578, 1225, and 580	O–H (H_2O), C═C (aromatic), C–O (epoxy), and Fe–O	Fe–O peak at 580 cm^{-1} appears in Fe_3O_4/GO but not in GO	20
6	Magnetic GOs	3450, 1730, 1620, 1220, and 1100	O–H (adsorbed water), C═O, C═C (skeletal), O═C–O (carboxyl), and C–O (alkoxy)	Broad –OH stretching; oxygen-containing groups confirmed	54
7	Magnetic PANI/ GO	3400, 1750, 1630, 1420, 1180, 790, and 585	–OH, C═O, C═C, C–C, C–O/N, and Fe–O	Fe–O bands at 790 & 585 cm^{-1} confirm magnetite	17
8	EDTA–mGO	3435, 3260, 1733, 1401, 1384, 1122, and 581	–OH, –NH, C═O, C–N, C–OH, C–NH_2, and Fe–O	GO C═O (1726) shifts to 1564 in mGO (COO^-)	21
9	Magnetic Fe_3O_4/ graphene	3450, 1625, 1251, and 580	–OH, C–O, CO–H, and Fe–O	Intensity of –OH and Fe–O decreased in the composite	12
10	UiO-66/Fe_3O_4/ GO	3423, 1577–1654, 1095, and 571	–OH, C═C, C–O, and Fe–O	Intensity of –OH, Fe–O increased	19
11	PMMA/GO–Fe_3O_4	3430, 1730, 1444, 1244, and 584	–CH_2 stretching vibrations, C═O stretching, bending vibration of the C–H bonds of the –CH_3 group, and C–O–C stretching vibration	Fe–O peak at 584 cm^{-1} appears in PMMA/GO–Fe_3O_4	53
12	Fe_3O_4/RGO	1642, 675	–COOH, Fe–O	Stretching vibration of Fe–O bond is also shifted to 675 cm^{-1} compared to that of 570 cm^{-1} reported for the stretching mode of Fe–O in bulk Fe_3O_4	35

rational design of next-generation sorbents with enhanced selectivity and capacity. The primary mechanisms at play are discussed in this section.

5.2.1 Electrostatic attraction. The surface of GO and rGO is densely populated with oxygen-containing functional groups (*e.g.*, carboxyl, hydroxyl, epoxy). Under typical environmental pH conditions (neutral or slightly acidic), the carboxyl and hydroxyl groups are deprotonated, resulting in a significant negative charge on the graphene surface. This negative surface charge facilitates a strong, long-range electrostatic attraction of

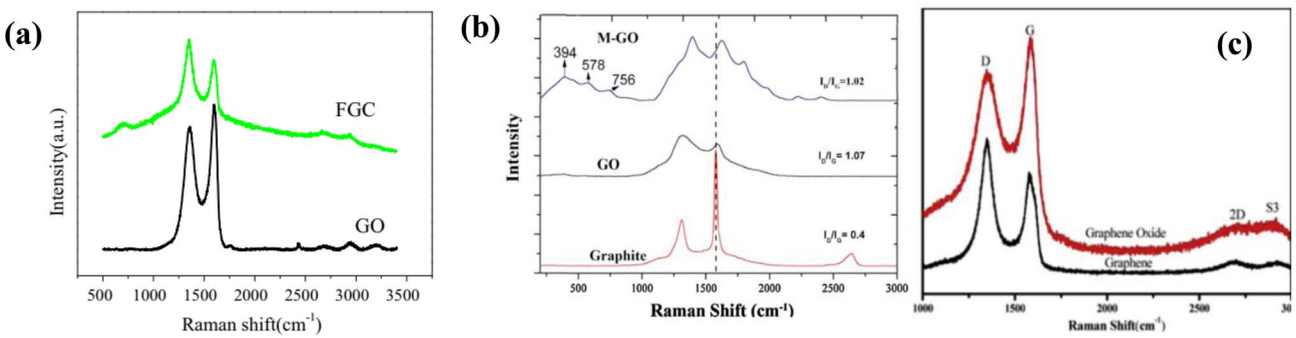

Fig. 14 Representative Raman spectra of magnetic graphene derivatives (a) GO and Fe_3O_4/graphene, (b) graphite, GO, and Fe_3O_4/GO, and (c) graphene and GO.[12,33,54]

Table 7 Summary of Raman spectral characteristics of various Fe_3O_4@graphene-based NCs

No.	Material	D-Band (cm^{-1})	G-Band (cm^{-1})	I_D/I_G	Remarks for I_D/I_G	Ref.
01	SMGO	~1356	~1603	1.28	Presence of localized sp^3 defects	38
02	CMC/MGOs	1332	1580–1602	1.06	Notably increased after using the plasma-grafted technique	1
03	Magnetic GOs	1350	1580	0.83	Indicate the defects of magnetic GOs	54
04	Fe_3O_4/graphene	~1355	~1597	1.11	New graphitic domains created	12
05	Fe_3O_4/graphene	1344	1582	0.92	Indicating the existence of graphitic carbon	59
06	M-GO hybrid	1350	1580	1.02	Anchoring of the magnetite NPs to the surface of graphene	33
07	Fe_3O_4@GO	1352	1582	0.89 ± 0.01	Increase in defects on the GO sheet due to the attachment of Fe_3O_4	41
08	Magnetic anatase–GO NC	1345	1585			46
09	rGO@Fe_3O_4	1345	1570	1.01	Representing an increase of defect density	61
10	M-GO	1346	1595	1.0	Increased intensity of both D and G bands attributed to the presence of Fe_3O_4	60
11	rGO/Fe_3O_4	1334	1600			42
12	Binary ferberite–graphene NCs	1345	1603			28
13	rGO/Fe_3O_4	1306.92	1591	1.19	Magnetite NPs were decorated on the surfaces of rGO sheets	62
14	rGO/Fe_3O_4	1341	1596			16
15	GO–MGH–chitosan	1295–1347	1596–1609	1.16	Involvement of oxygen-containing groups with the functional groups of CS and MGH	69

positively charged radionuclide species, such as the hydrated cations UO_2^{2+}, Cs^+, and Sr^{2+}, drawing them from the bulk solution to the sorbent surface.[74]

5.2.2 Surface complexation. Beyond simple electrostatic attraction, oxygen-containing functional groups can act as powerful Lewis bases (ligands), forming stable coordination complexes with radionuclide ions. It can occur *via* the formation of inner-sphere complexes, in which the radionuclide ion binds directly to the surface functional groups without intervening water molecules, or outer-sphere complexes, in which the ion remains fully or partially hydrated and is bound *via* electrostatic forces. This mechanism is particularly dominant for actinides such as U(VI) and Th(IV), which have a high affinity for oxygen-donating ligands.[3,74]

5.2.3 Ion exchange. The protons on the acidic carboxyl and hydroxyl groups, or other mobile counter-ions (like Na^+ or K^+) present on the NC surface, can be stoichiometrically exchanged for radionuclide ions from the solution. This mechanism is particularly relevant for the sorption of alkali and alkaline earth metals, such as Cs^+ and Sr^{2+}, which have a lower tendency to form strong covalent complexes.[6,27]

5.2.4 Physical sorption and coagulation. The vast, delocalized π-electron system and the high specific surface area of the graphene sheets provide numerous sites for weaker physical sorption forces, such as van der Waals interactions. Furthermore, GO has been observed to act as a coagulant, effectively enmeshing and precipitating certain radionuclides, thereby contributing to their removal from the aqueous phase.[3,14] The magnetic core of the NC then facilitates the rapid aggregation and magnetic separation of these coagulates.[30]

5.3 Key factors influencing sorption efficiency

The practical performance of Fe_3O_4@graphene NCs as sorbents is highly susceptible to various operational parameters. Optimizing these factors is crucial for achieving maximum removal efficiency in real-world applications.

5.3.1 pH of the solution. The solution pH is arguably the most critical factor, as it simultaneously governs the sorbent's surface charge (specifically, its relationship to the point of zero charge, PZC) and the chemical speciation of the dissolved radionuclides. For U(VI), sorption is typically optimal at slightly acidic to neutral pH values of 4.0–7.0. At lower pH, the high concentration of H^+ ions protonates the sorbent surface, leading to electrostatic repulsion with the cationic UO_2^{2+} species and intense competition for binding sites. At higher pH levels (>7.0), uranium speciates into stable, anionic uranyl carbonate or hydroxide complexes, which are repelled by the negatively charged sorbent surface, thereby reducing sorption.[4,12,49,73] In contrast, the sorption of monovalent Cs^+ is generally favored at neutral to alkaline pH, where the sorbent surface is more strongly deprotonated and negatively charged, and competition from H^+ ions is minimal.[19,25]

5.3.2 Initial ion concentration. The efficacy and kinetics of the sorption process are critically influenced by the initial concentration of the target radionuclide and the contact time between the sorbent and the contaminated solution. The initial concentration establishes the driving force for mass transfer from the aqueous phase to the sorbent surface. Generally, the sorption capacity increases with a higher initial ion concentration, as more ions are available to occupy the active binding sites. However, this trend continues only until the sorbent reaches saturation, at which point the capacity plateaus. The

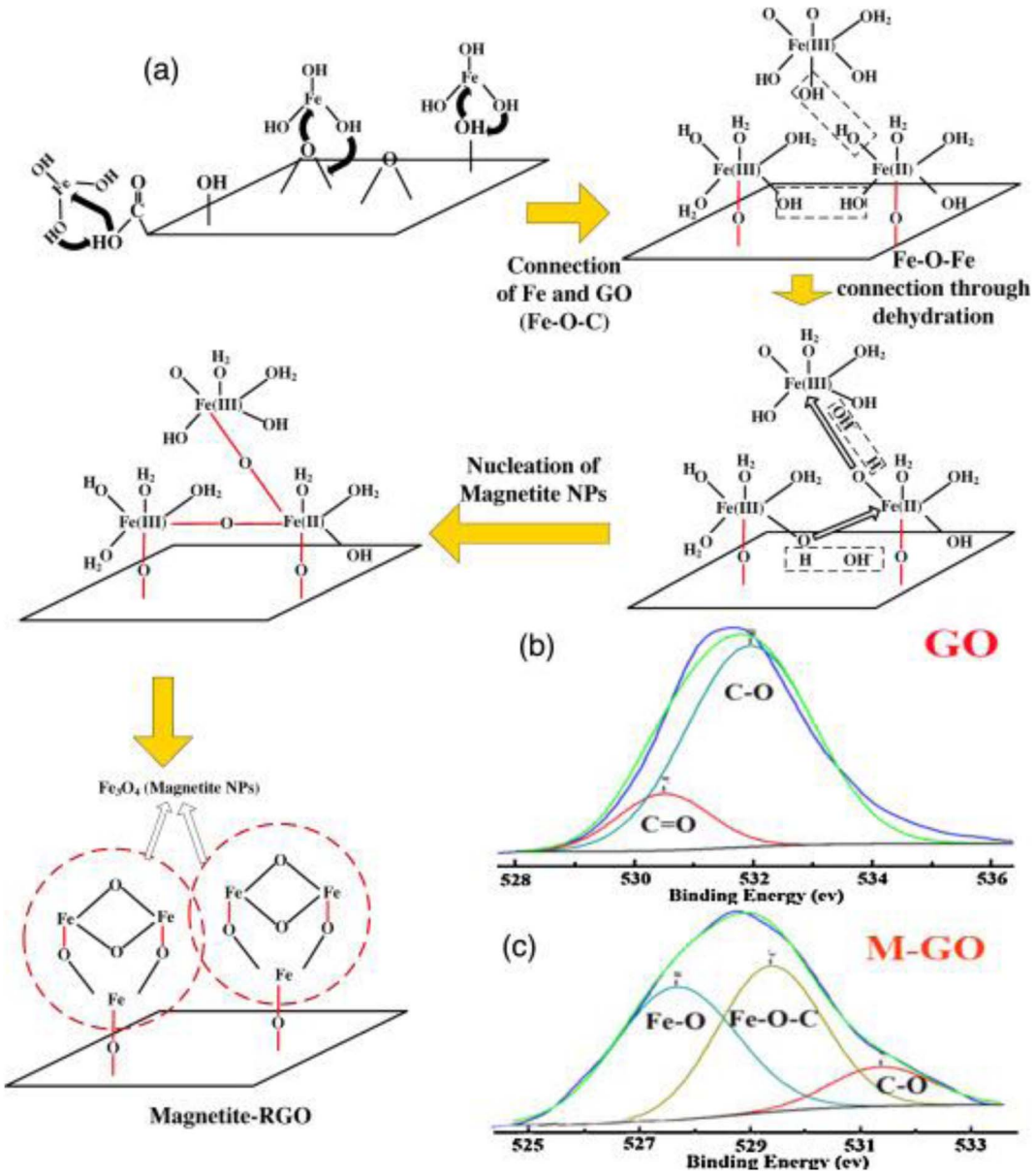

Fig. 15 (a) Proposed mechanism for the formation of Fe_3O_4 NPs on the GO surface, highlighting the formation of Fe–O–C bonds. High-resolution XPS O 1s spectra of (b) GO and (c) the M-GO composite, where the appearance of a peak corresponding to Fe–O–C confirms the chemical bonding.[33]

relationship between initial concentration and equilibrium uptake is often modeled using sorption isotherms, such as the Langmuir or Freundlich models.[13,18,43] For instance, studies on a magnetic graphene oxide NC showed that for an initial Sr^{2+} concentration range of 25–125 mg L^{-1}, the maximum sorption (29.98%) was achieved at 50 mg L^{-1}, while for Cs^+ in a range of 200–500 mg L^{-1}, the peak removal (57.2%) occurred at 250 mg L^{-1}.[43] Similarly, the sorption of Th(IV) on magnetic graphene oxide nanoribbons (MGONRs) increased with initial concentrations from 5 to 150 mg L^{-1}, reaching a maximum capacity of 31.4 mg g^{-1} at 150 mg L^{-1}.[13] For Cs^+ removal using a UiO-66/Fe_3O_4/GO composite, the sorption capacity peaked at 60 mg g^{-1} when the initial concentration was 100 mg L^{-1}.[19]

5.3.3 Contact time. The contact time required to reach sorption equilibrium is another crucial parameter that varies with the specific radionuclide, its initial concentration, and the sorbent properties. The sorption process is typically biphasic, beginning with a rapid initial uptake phase in which radionuclides are adsorbed onto readily accessible external surface sites. It is followed by a much slower, diffusion-controlled phase as the ions gradually migrate into the composite's interior porous structure. For example, a GO/Fe_3O_4/GC composite demonstrated high-speed kinetics for U(VI), removing over 98% within 30 min.[49] In another case, a rGO/Fe_3O_4/TW composite adsorbed 96% of U(VI) in under one minute, although it took 2 h to reach final equilibrium.[73] In contrast, the sorption of Th(IV) onto MGONRs was slower, reaching equilibrium after 6 h.[13] For

Table 8 Summary of elemental composition and chemical state information for Fe_3O_4@graphene-based NCs from XPS analysis

No.	Composite name	Element	XPS peak	Binding energy (eV)	Chemical state	Ref.
1	Fe_3O_4/GO	C, O, Fe	C 1s, O 1s, Fe $2p_{3/2}$, Fe $2p_{1/2}$	C 1s: 285.0, O 1s: 530.4, Fe $2p_{3/2}$: 711.12, Fe $2p_{1/2}$: 724.79	C–C/C=C (sp^2) Anionic O^{2-} from Fe_3O_4 Fe^{2+}/Fe^{3+} (Fe_3O_4 phase)	55
2	SMGO	C, O, Fe	C 1s, O 1s, Fe $2p_{3/2}$, Fe $2p_{1/2}$	C 1s: 284.5 (C–C), 286.0 (C–O), 288.2 (C=O), O 1s: 531.4 (Fe_3O_4), 533.0 (C=O), 533.5 (C–O), Fe 2p: 710.7, 713.0 (Fe^{2+}, Fe^{3+}), 724.4, 726.6 (Fe^{2+}, Fe^{3+}), 719.3, 733.3 (satellites from γ-Fe_2O_3)	C–C (sp^2), C–O (hydroxyl/epoxy), C=O (carbonyl/carboxyl) O^{2-} in Fe_3O_4 Fe^{2+}/Fe^{3+} in Fe_3O_4, minor γ-Fe_2O_3 contribution	38
3	EDTA–mGO	Fe, N	Fe 2p, N 1s	Fe 2p: 710.2, N 1s: 400.3	Fe^{3+} in Fe_3O_4 –NH or –N in EDTA anchored to mGO	21
4	Fe_3O_4/graphene	Fe, O	Fe 2p, O 1s	Fe $2p_{3/2}$: 710.1, Fe $2p_{1/2}$: 724.3, O 1s: 530.1 (O^{2-}), 531.5 (–COOH), 532.1 (–OH)	Fe_3O_4 (Fe^{2+}/Fe^{3+}) Oxygen in iron oxide, carboxylic acid, and hydroxyl groups	12
5	PB/Fe_3O_4/GO	C, O, N, Fe	C 1s, Fe 2p, N 1s	C 1s: 284.7 (C–C/C=C), 285.6 (C–O), 286.8 (C=O), 287.6 (C≡N), 288.9 (O–C=O), Fe $2p_{3/2}$: 711.3, Fe $2p_{1/2}$: 724.8, N 1s: 399.0, 398.6, 397.3	Aromatic C, epoxy, carbonyl, cyano group (C≡N), carboxyl Fe_3O_4 $[Fe(CN)_6]^{4-}$ cyano nitrogen	31
6	M-GO	C, O, Fe	C 1s, O 1s, Fe 2p	C 1s: 285.0 (C–C/C=C), 286.2 (C–OH), 287.1 (C–O–C), 289.1 (O–C=O), Fe 2p: ~711.0, O 1s: 532.0	Magnetic Fe_3O_4 presence confirmed (Fe 2p ~ 711 eV) Oxygen functional groups reduced (~55%)	33
7	GO–Fe_3O_4	C, O, Fe	C 1s, O 1s, Fe $2p_{3/2}$, Fe $2p_{1/2}$	C 1s: ~285.0, O 1s: ~530.0, Fe $2p_{3/2}$: 711.12, Fe $2p_{1/2}$: 724.79	sp^2 carbon (C–C/C=C). Oxygenated groups Fe_3O_4 (Fe^{2+}/Fe^{3+})	43
8	rGO/Fe_3O_4	C, O, Fe	C 1s, O 1s, Fe $2p_{3/2}$, Fe $2p_{1/2}$	C 1s: 284.4 (C–C/C=C), 287.4 (C=O), Fe 2p: 711.1 ($2p_{3/2}$), 724.7 ($2p_{1/2}$), O 1s: 530.5 (Fe–O), 532.0 (C=O), 533.4 (C–O)	Graphene backbone (C–C), carbonyl Fe_3O_4 confirmed *via* Fe 2p, with Fe–O anchoring to rGO and oxygenated groups	61
9	rGO/Fe_3O_4	C, O, Fe	Fe 2p, O 1s, C 1s	Typical Fe $2p_{3/2}$. 710–711 eV (not restated here)	Fe_3O_4 and rGO functional groups	65
10	rGO/Fe_3O_4	C, O, Fe	C 1s, O 1s, Fe 2p	C 1s: 285, O 1s: 531, Fe 2p: 725	sp^2 C (graphene), oxygenated groups Fe_3O_4 phase	16
11	3D MPBRGO	C, O, N, Fe	C 1s, Fe 2p, N 1s	C 1s: 284.5 (C–C/C=C), 285.7 (C≡N, from $[Fe(CN)_6]^{4-}$), 286.5 (C–O), 287.8 (C=O), 288.9 (O–C=O), Fe 2p: 708.3 (Fe in PB), 711.3 (Fe_3O_4 $2p_{3/2}$), 724.9 (Fe_3O_4 $2p_{1/2}$), N 1s: 397.0, 398.0, 399.2	sp^2 C (graphene), cyano group (PB), epoxy, carbonyl, carboxylic Prussian blue ($[Fe(CN)_6]^{4-}$), magnetite (Fe_3O_4) Cyano nitrogen from $[Fe(CN)_6]^{4-}$	45
12	PB/Fe_3O_4/GO	C, O, N, Fe	C 1s, Fe 2p, N 1s	C 1s: 284.8 (C=C/C–C/C–H), 285.8 (C–O), 286.8 (C=O), 287.6 (C≡N), 288.9 (O–C=O), Fe 2p: 711.3 (Fe $2p_{3/2}$), 724.8 (Fe $2p_{1/2}$), 708.3 (Fe $2p_{3/2}$ in $[Fe(CN)_6]^{4-}$), N 1s: 397.5, 398.4, 399.6	Aromatic graphitic carbon, epoxy, carbonyl, nitrile (C≡N), and carboxylic groups Fe_3O_4 (magnetite) and Prussian blue ($[Fe(CN)_6]^{4-}$) coexist C≡N from $[Fe(CN)_6]^{4-}$confirming PB presence	25

Cs^+ sorption on a UiO-66/Fe_3O_4/GO composite, 50% of the removal occurred within the first 10 min, with equilibrium being approached after 2 h.[19] These examples highlight the rapid sorption kinetics characteristic of these materials, a key advantage for practical water treatment applications.

5.3.4 Temperature. The influence of temperature on the sorption process provides valuable thermodynamic insight. For many radionuclides, sorption onto these composites is endothermic, meaning that increasing temperature enhances sorption capacity. It can be attributed to several factors, including an increase in the diffusion rate of the ions from the bulk solution to the sorbent surface, potential swelling or changes in the sorbent's pore structure at higher temperatures, and an increase in the chemical activity and mobility of the radionuclide species in solution.[12,17,19,20,25,73]

5.3.5 Presence of competing ions. Real-world wastewater is rarely a simple solution of a single contaminant. It is typically a complex matrix of coexisting ions that can compete with the target radionuclides for active sorption sites, thereby reducing overall removal efficiency. Cations with a higher charge density (*e.g.*, Al^{3+}, Ca^{2+}) or a smaller hydrated radius often exhibit stronger competition and can significantly reduce the removal efficiency for the target radionuclide. For example, the presence of common groundwater ions, such as K^+ and Na^+, can slightly decrease Cs^+ sorption, whereas trivalent cations, such as Al^{3+}, can significantly inhibit U(VI) sorption.[19,26,49] Conversely, the presence of certain anions, such as CO_3^{2-}, can in some cases enhance sorption by modifying the sorbent surface charge or by forming ternary surface complexes.[10]

Table 9 Summary of thermal stability and decomposition behavior of Fe_3O_4@graphene-based NCs from TGA analysis

No.	Material	Stage	Temp. range (°C)	Weight loss (%)	Interpretation	Ref.
01	CMC/MGOs	1	120–350	73		1
02	EDTA–mGO	1	Before 200		Absorbed water	21
		2	Higher than 200		Decomposition of EDTA	
03	FGC	1	30–720	18.3	Oxygen functional groups	12
		2	735–772	26.8	Carbon skeleton	
04	Fe_3O_4/graphene	1	Till 300	0.03	Evaporation of trace H_2O	59
		2	350–500		Organic molecules	
		3	After 500		Formation of Fe_3O_4	
05	PB/Fe_3O_4/GO	1	Below 150		Loss of water	31
		2	Around 200		Removal of coordinating water, oxygen functional groups	
		3	300–550		Combustion of GO and the decomposition of the cyano group	
		4	Elevated to 950		Pyrolysis of the carbon skeleton	
06	NPs@GO	1	Below 120		Evaporation of adsorbed water	36
		2	At 200		Decomposition of labile oxygen-containing functional groups	
07	FGC	1	Below 120		Evaporation of adsorbed water molecules	30
		2	120–350		Oxygen-containing functional groups	
		3	350–520		Decomposition of the carbon skeleton	
08	Fe_3O_4@GO	1	At 120		Evaporation of adsorbed water	41
		2	120–300		Organic functional groups	
		3	300–600		Combustion of the carbon skeleton	
09	APS	1	200–400	28.4	Organic molecules are decomposed partially	46
		2	400–600	18	Siloxane bond breaking	
10	Fe_3O_4/RGO	1	At 100		Loss of moisture	65
		2	150–400		Functional group	
		3	400–500		rGO was converted into carbon dioxide, and Fe_3O_4 was completely oxidized into Fe_2O_3	
		4	After 500		Fe_2O_3 particles	

6.0 Challenges and future perspectives

6.1 Current challenges

While the scientific literature convincingly demonstrates the significant promise of Fe_3O_4@graphene NCs, several formidable challenges must be systematically addressed to facilitate the transition of this technology from the controlled environment of the laboratory to large-scale, real-world industrial applications. Overcoming these issues will be the central focus of future research and development in this field.

6.1.1 Scalability and cost-effectiveness. A significant impediment to commercialization is the scalability of production. Many of the current synthesis methods reported in the literature are complex, time-consuming, multi-step processes that are difficult to scale up while maintaining high quality and batch-to-batch reproducibility. Furthermore, they often rely on expensive and hazardous precursor materials, notably high-purity GO and various chemical reagents.[75–77] Developing simple, continuous, and economically viable production processes is a prerequisite for the practical implementation.

6.1.2 Long-term stability and durability. The performance of these NCs must be reliable and predictable over extended operational periods and under harsh, variable chemical conditions (*e.g.*, extreme pH, high salinity, presence of oxidizing/reducing agents) characteristic of many radioactive waste streams.[78–80] Ensuring the long-term structural, chemical, and mechanical stability of the material and preventing the leaching of embedded iron oxide NPs remain key challenges.

6.1.3 Selective sorption. Real-world effluents are chemically complex, containing a diverse mixture of coexisting ions (*e.g.*, Na^+, K^+, Ca^{2+}, Mg^{2+}) that are often present at concentrations orders of magnitude higher than the target radionuclides. These ions can compete for active sorption sites, significantly reducing the efficiency and capacity for radionuclide removal.[80,81] Enhancing the intrinsic selectivity of the NCs for specific high-risk contaminants, such as cesium-137 or strontium-90, is a major scientific and engineering hurdle.

6.1.4 Environmental and health impact. A comprehensive and rigorous life-cycle assessment of these nanomaterials is urgently required. The potential for the unintended release and leaching of the constituent NPs into the environment during use, regeneration, or final disposal must be thoroughly investigated. The long-term toxicity and ecological impact of these materials are still not fully understood,[82] and it is imperative to ensure that the proposed remediation solution does not inadvertently create a new environmental problem.

Table 10 Summary of magnetic properties of various Fe_3O_4@graphene-based NCs from VSM analysis

No.	Material	M_s (emu g^{-1})	M_r (emu g^{-1})	Magnetic behavior	Ref.
01	Fe_3O_4/GO	48.6	0.785	Super-paramagnetic	55
02	MGOC	22.55			47
03	SMGO	41.38	3.5	Super-paramagnetic	38
04	MGONRs	33.7	Neglectable		13
05	mGO–PP	14.63			68
06	EDTA–mGO	39.47			21
07	Fe_3O_4/graphene	45.6			12
08	UiO-66/Fe_3O_4/GO	15.53			19
09	Fe_3O_4/RGO (5 : 1)	10			35
	Fe_3O_4/RGO (9 : 1)	24			
10	Fe_3O_4–NH_2/GO (3 : 1)	58.26	0	Super-paramagnetic	50
11	M-GO (stirred method)	41			33
	M-GO (ultrasound method)	30			
12	Fe_3O_4@GO	40.4		Super paramagnetic	41
13	mGOi	65		Super-paramagnetic	56
14	M-GO	10.74			43
15	Fe_3O_4@GO	16.4		Super-paramagnetic	70
16	TBOT–GO–Fe_3O_4 (hydrothermal)	5.8	0.42	Super-paramagnetic	46
	TBOT–GO–Fe_3O_4 (sol–gel)	2.8	0.20	Super-paramagnetic	
17	MGO	5.76	0	Super-paramagnetic	71
18	Mag GO	36.77	0	Super-paramagnetic	72
19	MGO	17.38	Nearly zero	Super-paramagnetic	57
20	RGO/Fe_3O_4	12.6	0	Super paramagnetic	42
21	GN–Fe_3O_4	10.23	0.03	Super-paramagnetic	58
22	rGO/Fe_3O_4	42		Super-paramagnetic	62
23	rGO/Fe_3O_4	18.6	Low	Super-paramagnetic	16
24	MNGO	10.74		Super-paramagnetic	67
25	rGO/Fe_3O_4/TW	10		Super-paramagnetic	73
26	Fe_3O_4/GO	31.2			4
27	MCGO	30.21			40
28	M/GO	31			52

6.2 Future research directions

Future research efforts should be strategically directed at overcoming the challenges mentioned above through concerted innovation in material design, process engineering, and safety assessment.

6.2.1 Advanced and sustainable synthesis. There is a pressing need to develop and validate green, sustainable synthesis routes that use non-toxic, renewable, and low-cost precursors. The implementation of advanced manufacturing processes, such as continuous flow reactors or aerosol-based synthesis, could dramatically enhance scalability, reduce production costs, and improve the consistency and quality of the final product.[83,84]

6.2.2 Tailored surface functionalization and hierarchical design. A highly promising avenue for future research is the rational design of the NC surface to create binding sites with exceptionally high affinity and selectivity for specific target radionuclides. This could involve advanced surface engineering techniques such as grafting specific chelating agents, developing ion-imprinted polymers on the surface, or creating hierarchical composites with other advanced materials like metal–organic frameworks (MOFs).[85,86]

6.2.3 Process optimization and predictive modeling. Systematic optimization of the entire sorption-desorption process is needed to maximize performance and minimize operational costs. The increasing use of advanced computational tools, such as density functional theory (DFT) and molecular dynamics (MD) simulations, can provide unprecedented insights into sorption mechanisms at the molecular level.[87,88] This fundamental understanding can, in turn, guide the rational design of more effective and efficient sorbent materials.

6.2.4 Sustainable and efficient regeneration strategies. The long-term sustainability of this technology depends on the ability to regenerate and reuse the sorbent multiple times. Research into novel, less chemically intensive regeneration methods, such as electrochemical desorption, thermal swing, or microwave-assisted desorption, could significantly enhance overall efficiency and reduce secondary waste generated during regeneration.[78] The primary goal is to develop strategies that allow for dozens or even hundreds of reuse cycles without a significant loss of performance.

6.2.5 Integration and system-level development. Future work should move beyond batch-scale experiments and focus on integrating these magnetic NCs into practical, continuous-flow water treatment systems. It could involve their use in magnetically stabilized fluidized-bed reactors, incorporation into reactive membrane systems, or deployment in packed-bed columns.[89,90] Developing portable, modular, and scalable

Table 11 Summary of the sorption performance of various magnetic graphene derivatives for the removal of radionuclides[a]

Materials	Tested radionuclides	Sorption conditions	Kinetic model, isotherm model	Maximum sorption capacity	Ref.
CMC/MGOs	U(VI)	pH = 5.5, T = 301 K, t = 24 h	Pseudo-second-order, Langmuir	7.94×10^{-4} mol g^{-1}	1
Fe_3O_4/GO	U(VI)	pH = 5.5, T = 293 K, t = 24 h	Pseudo-second-order, Langmuir	69.49 mg g^{-1}	4
PB/Fe_3O_4/GO	Cs(I)	pH = 7.0, T = 298 K, t = 24 h	Pseudo-second-order, Langmuir	55.56 mg g^{-1}	25
Fe_3O_4/GO	U(VI)	pH = 5.5, T = 298 K, t = 40 min	Pseudo-second-order, Langmuir	176.47 mg g^{-1}	12
Fe_3O_4/GO	Th(IV)	pH = 3.0, T = 298 K, t = 6 h	Pseudo-second order, Freundlich	36.54 mg g^{-1}	13
Fe_3O_4/PANI/GO	Sr(II)	pH = 3.0, T = 293 K, t = 24 h	Pseudo-second-order, Langmuir	37.17 mg g^{-1}	17
rGO/Fe_3O_4	Cs(I) Sr(II)	pH = 7.0, T = 298 K, t = 6 h	Pseudo-second-order, Freundlich	128.2 mg g^{-1} 384.6 mg g^{-1}	16
UiO-66/Fe_3O_4/GO	Cs(I)	pH = 7.0, T = 298 K, t = 12 h	Pseudo-second-order, Langmuir	62.07 mg g^{-1}	19
Fe_3O_4/GO	U(VI)	pH = 5.0, T = 318 K, t = 5 h	Pseudo-second-order, Langmuir	3.50×10^{-4} mol g^{-1}	20
Fe_3O_4/EDTA/GO	U(VI)	pH = 5.5, T = 298 K, t = 100 min	Pseudo-second-order, Langmuir	277.43 mg g^{-1}	21
Fe_3O_4/PB/GO	Cs(I)	pH = 7.0, T = 298 K, t = 24 h	Langmuir	362 mg g^{-1}	26
$FeWO_4$/GO	U(VI)	pH = 6.0, T = 298 K, t = 1–2 h	Pseudo-second-order, Langmuir	455 mg g^{-1} (1 h) 625 mg g^{-1} (2 h)	28
PB/Fe_3O_4/GO	Cs(I)	pH = 7.0, T = 298 K, t = 24 h	Pseudo-second-order, Langmuir	43.52 mg g^{-1}	31
Fe_3O_4/GO	Sr(II)	pH = 7.0, T = 298 K, t = 5 h	Pseudo-second-order, Langmuir	13.7 mg g^{-1}	33
Fe_3O_4/chitosan/GO	U(VI)	pH = 5.0, T = 313 K, t = 100 min	Pseudo-second-order, Langmuir	204.1 mg g^{-1}	40
GO–Fe_3O_4	Cs(I) Sr(II)	pH = 10, pH = 4.0, T = 298 K, t = 2 h	Pseudo-second-ordered, Dubinin–Radushkevich, Freundlich	148.77 mg g^{-1} 17.92 mg g^{-1}	43
Fe_3O_4/PB/GO aerogel	Cs(I)	pH = 7.0, T = 303 K, t = 24 h	Pseudo-second-order, Langmuir	484.12 mg g^{-1}	45
Fe_3O_4/chitosan/GO	Co(II)	pH = 7.0, T = 298 K, t = 6 h	Pseudo-second-order, Langmuir	59.82 mg g^{-1}	47
GO/Fe_3O_4/GC	U(VI)	pH = 5.0, T = 298 K, t = 30 min	Pseudo-second-order, Langmuir	390.70 mg g^{-1}	49
Fe_3O_4/GO	Sr(II), Cs(I)	pH = 4.0, T = 293 K, t = 24 h	Pseudo-second-order, Langmuir	14.706 mg g^{-1} 9.259 mg g^{-1}	54
rGO/Fe_3O_4/TW	U(VI)	pH = 5.0, T = 298 K, t = 24 h	Pseudo-second-order, Langmuir	104.95 mg g^{-1}	73

[a] PB, Prussian blue; PANI, polyaniline.

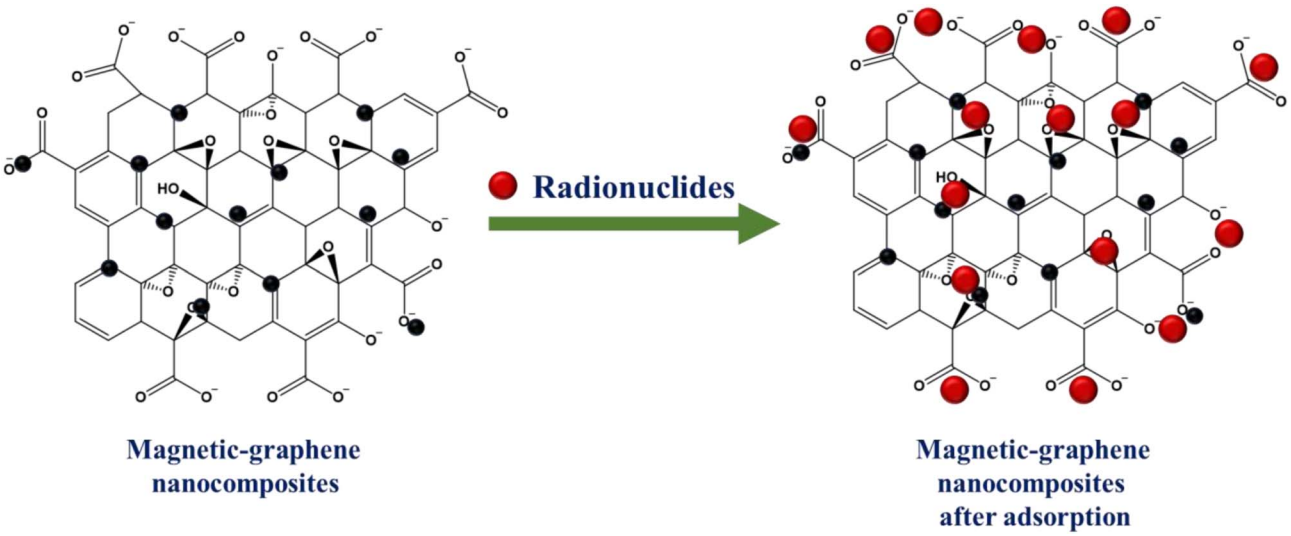

Fig. 16 Schematic representation of the primary mechanisms for radionuclide removal by magnetic-graphene NCs, including electrostatic attraction, surface complexation, and ion exchange.

systems for on-site treatment could provide rapid and practical solutions for the remediation of contaminated sites.

6.2.6 Comprehensive safety assessment and regulatory frameworks. A concerted effort is required to conduct comprehensive toxicological and ecotoxicological studies to ensure the safe application of these materials throughout their entire life cycle. The data is essential for establishing clear, robust regulatory guidelines for the production, handling, use, and ultimate disposal of these NCs, which will be critical for gaining public acceptance and facilitating their widespread, responsible adoption.[91]

7.0 Conclusion

Magnetic NCs based on Fe_3O_4@graphene derivatives represent a significant and auspicious advancement in materials science, poised to address some of the most pressing challenges in radioactive waste management. Their unique and rationally designed architecture, which combines the vast, functionalizable surface of a graphene matrix with the powerful magnetic responsiveness of embedded Fe_3O_4 NPs, results in a multifunctional sorbent capable of efficiently capturing and removing a wide range of hazardous radionuclides from contaminated environments. This review systematically examines the key facets of these advanced materials, from the nuances of their synthesis and characterization details to the fundamental mechanisms that govern their sorptive performance. The high efficacy of these composites is clearly driven by a powerful synergy of electrostatic attraction, surface complexation, and ion exchange, with their practical performance being highly dependent on the optimization of operational conditions such as pH, temperature, and the composition of the aqueous matrix. Despite their well-demonstrated potential, the path from promising laboratory-scale materials to practical large-scale implementation is contingent on overcoming several significant and interconnected challenges. Critical issues of scalable, cost-effective synthesis, ensuring long-term stability and durability in harsh chemical environments, and, perhaps most importantly, enhancing sorption selectivity in complex, multi-component ionic matrices remain paramount. Furthermore, a rigorous assessment of their potential environmental and health impacts throughout their life cycle is essential for responsible, sustainable technological development. Future research must therefore be strategically focused on innovative and green synthesis techniques, the rational design of surface functionalities for highly targeted radionuclide capture, and the development of robust and efficient regeneration protocols. By systematically addressing these challenges through interdisciplinary research, Fe_3O_4@graphene NCs can evolve from a scientific curiosity into a pivotal, deployable technology for mitigating the pervasive risks of radioactive contamination, thereby contributing to a safer, more sustainable future.

Conflicts of interest

The authors declare that they have no known competing financial interests or personal relationships that could have appeared to influence the work reported in this paper.

Data availability

All data generated or analyzed during this study are included in this article.

Acknowledgements

Funding for this research was provided by the Japan Society for the Promotion of Science (JSPS) KAKENHI (Grant No. 24K15337 to IR), the Research and Innovation Centre (RIC) at Khulna University (Memo No. KU/RIC-04/2000-323 to MM & IR), and the Environmental Radioactivity Research Network Center (ERAN) at Fukushima University (Grant No. I-25-10 to MM & IR). During manuscript preparation, Gemini Advanced, QuillBot, and Grammarly were employed to assist with paraphrasing and language editing. The authors have verified the content and accept full responsibility for the published work.

References

1 P. Zong, D. Cao, Y. Cheng, S. Wang, J. Zhang, Z. Guo, T. Hayat, N. S. Alharbi and C. He, *Cellulose*, 2019, **26**, 4039–4060.
2 Q.-H. Hu, J.-Q. Weng and J.-S. Wang, *J. Environ. Radioact.*, 2010, **101**, 426–437.
3 A. Yu. Romanchuk, A. S. Slesarev, S. N. Kalmykov, D. V. Kosynkin and J. M. Tour, *Phys. Chem. Chem. Phys.*, 2013, **15**, 2321.
4 P. Zong, S. Wang, Y. Zhao, H. Wang, H. Pan and C. He, *Chem. Eng. J.*, 2013, **220**, 45–52.
5 H. Yang, L. Sun, J. Zhai, H. Li, Y. Zhao and H. Yu, *J. Mater. Chem. A*, 2014, **2**, 326–332.
6 A. Y. Romanchuk, A. S. Kuzenkova, A. S. Slesarev, J. M. Tour and S. N. Kalmykov, *Solvent Extr. Ion Exch.*, 2016, **34**, 594–602.
7 D. Lux, L. Kammerer, W. Rühm and E. Wirth, *Sci. Total Environ.*, 1995, **173–174**, 375–384.
8 M. Chino, H. Nakayama, H. Nagai, H. Terada, G. Katata and H. Yamazawa, *J. Nucl. Sci. Technol.*, 2011, **48**, 1129–1134.
9 W. M. A. El Rouby, A. A. Farghali, M. A. Sadek and W. F. Khalil, *J. Inorg. Organomet. Polym. Mater.*, 2018, **28**, 2336–2349.
10 P. Wu, Y. Wang, Y. Li, X. Hu, T. Xiu, D. Yuan, Y. Liu, Z. Wu and Z. Liu, *J. Radioanal. Nucl. Chem.*, 2019, **322**, 553–559.
11 X. Wang, Z. Chen and X. Wang, *Sci. China: Chem.*, 2015, **58**, 1766–1773.
12 D. Zhao, H. Zhu, C. Wu, S. Feng, A. Alsaedi, T. Hayat and C. Chen, *Appl. Surf. Sci.*, 2018, **444**, 691–698.
13 P. Wu, Y. Wang, X. Hu, D. Yuan, Y. Liu and Z. Liu, *J. Radioanal. Nucl. Chem.*, 2019, **319**, 1111–1118.
14 L. Xu and J. Wang, *Crit. Rev. Environ. Sci. Technol.*, 2017, **47**, 1042–1105.
15 X. Wang, S. Yu, J. Jin, H. Wang, N. S. Alharbi, A. Alsaedi, T. Hayat and X. Wang, *Sci. Bull.*, 2016, **61**, 1583–1593.
16 C. R. Minitha, R. Suresh, U. K. Maity, Y. Haldorai, V. Subramaniam, P. Manoravi, M. Joseph and R. T. Rajendra Kumar, *Ind. Eng. Chem. Res.*, 2018, **57**, 1225–1232.
17 B. Hu, M. Qiu, Q. Hu, Y. Sun, G. Sheng, J. Hu and J. Ma, *ACS Sustain. Chem. Eng.*, 2017, **5**, 6924–6931.
18 G. Lujanienė, S. Šemčuk, I. Kulakauskaitė, K. Mažeika, D. Valiulis, R. Juškėnas and S. Tautkus, *J. Radioanal. Nucl. Chem.*, 2016, **307**, 2267–2275.
19 S. Feng, Z. Ni, S. Feng, Z. Zhang, S. Liu, R. Wang and J. Hu, *J. Radioanal. Nucl. Chem.*, 2019, **319**, 737–748.
20 D. Zhao, L. Chen, M. Sun and F. Li, *J. Radioanal. Nucl. Chem.*, 2015, **306**, 221–229.

21 D. Zhao, Q. Zhang, H. Xuan, Y. Chen, K. Zhang, S. Feng, A. Alsaedi, T. Hayat and C. Chen, *J. Colloid Interface Sci.*, 2017, **506**, 300–307.
22 J. Wang and S. Zhuang, *Rev. Environ. Sci. Bio/Technol.*, 2019, **18**, 231–269.
23 B. R. Figueiredo, S. P. Cardoso, I. Portugal, J. Rocha and C. M. Silva, *Sep. Purif. Rev.*, 2018, **47**, 306–336.
24 Y.-L. Choi, J.-S. Choi, L. P. Lingamdinne, Y.-Y. Chang, J. R. Koduru, J.-H. Ha and J.-K. Yang, *Environ. Sci. Pollut. Res.*, 2019, **26**, 22323–22337.
25 H. Yang, L. Sun, J. Zhai, H. Li, Y. Zhao and H. Yu, *J. Mater. Chem. A*, 2014, **2**, 326–332.
26 G. Lujanienė, S. Šemčuk, A. Lečinskytė, I. Kulakauskaitė, K. Mažeika, D. Valiulis, V. Pakštas, M. Skapas and S. Tumėnas, *J. Environ. Radioact.*, 2017, **166**, 166–174.
27 Y. Sun, D. Shao, C. Chen, S. Yang and X. Wang, *Environ. Sci. Technol.*, 2013, **47**, 9904–9910.
28 H. H. El-Maghrabi, S. M. Abdelmaged, A. A. Nada, F. Zahran, S. A. El-Wahab, D. Yahea, G. M. Hussein and M. S. Atrees, *J. Hazard. Mater.*, 2017, **322**, 370–379.
29 X. Xia, F. Zhou, J. Xu, Z. Wang, J. Lan, Y. Fan, Z. Wang, W. Liu, J. Chen, S. Feng, Y. Tu, Y. Yang, L. Chen and H. Fang, *Nat. Commun.*, 2022, **13**, 7247.
30 Y. Yao, S. Miao, S. Liu, L. P. Ma, H. Sun and S. Wang, *Chem. Eng. J.*, 2012, **184**, 326–332.
31 H. Yang, H. Li, J. Zhai, L. Sun, Y. Zhao and H. Yu, *Chem. Eng. J.*, 2014, **246**, 10–19.
32 H. Cong, J. He, Y. Lu and S. Yu, *Small*, 2010, **6**, 169–173.
33 A. Tayyebi, M. Outokesh, S. Moradi and A. Doram, *Appl. Surf. Sci.*, 2015, **353**, 350–362.
34 H. Yan, H. Li, X. Tao, K. Li, H. Yang, A. Li, S. Xiao and R. Cheng, *ACS Appl. Mater. Interfaces*, 2014, **6**, 9871–9880.
35 A. Mishra and T. Mohanty, *Mater. Today: Proc.*, 2016, **3**, 1576–1581.
36 P. Tancredi, O. Moscoso Londoño, P. C. Rivas Rojas, M. Knobel and L. M. Socolovsky, *Mater. Res. Bull.*, 2018, **107**, 255–263.
37 C. S. Biju, *Nano-Struct. Nano-Objects*, 2018, **13**, 44–50.
38 Y.-L. Choi, J.-S. Choi, L. P. Lingamdinne, Y.-Y. Chang, J. R. Koduru, J.-H. Ha and J.-K. Yang, *Environ. Sci. Pollut. Res.*, 2019, **26**, 22323–22337.
39 M. Llenas, S. Sandoval, P. M. Costa, J. Oró-Solé, S. Lope-Piedrafita, B. Ballesteros, K. T. Al-Jamal and G. Tobias, *Nanomaterials*, 2019, **9**, 1364.
40 G. Huang, W. Peng and S. Yang, *J. Radioanal. Nucl. Chem.*, 2018, **317**, 337–344.
41 S. Uten, P. Boonbanjong, Y. Prueksathaporn, K. Treerattrakoon, N. Sathirapongsasuti, N. Chanlek, S. Pinitsoontorn, P. Luksirikul and D. Japrung, *ACS Omega*, 2024, **9**, 2263–2271.
42 C. Prasad, P. K. Murthy, R. H. Krishna, R. S. Rao, V. Suneetha and P. Venkateswarlu, *J. Environ. Chem. Eng.*, 2017, **5**, 4374–4380.
43 S. Aytas, S. Yusan, S. Sert and C. Gok, *Charact. Appl. Nanomater.*, 2021, **4**, 26.
44 L. P. Lingamdinne and J. R. Koduru, *Environ. Anal. Ecol. Stud.*, 2018, **2**, 110–113.
45 H. Seema, *Arabian J. Chem.*, 2020, **13**, 4417–4424.
46 L. Zadmehr and S. Salem, *Mater. Sci. Eng., B*, 2021, **268**, 115122.
47 Y. Ouyang, J. Deng, Z. Chen, L. Yang, S. Xiao, L. Wang and Y. Zhao, *J. Radioanal. Nucl. Chem.*, 2020, **326**, 1699–1708.
48 R. Zhang, P. Su and Y. Yang, *J. Sep. Sci.*, 2014, **37**, 3339–3346.
49 A. Yang, Z. Wang and Y. Zhu, *Sci. Rep.*, 2021, **11**, 8440.
50 F. Ebrahimi-Tazangi, S. H. Hekmatara and J. Seyed-Yazdi, *J. Alloys Compd.*, 2019, **809**, 151779.
51 M. J. Molaei, *Mater. Sci. Eng., B*, 2021, **272**, 115325.
52 M. Liu, C. Chen, J. Hu, X. Wu and X. Wang, *J. Phys. Chem. C*, 2011, **115**, 25234–25240.
53 M. Rajabi, K. Mahanpoor and O. Moradi, *Composites, Part B*, 2019, **167**, 544–555.
54 D. Li, B. Zhang and F. Xuan, *J. Mol. Liq.*, 2015, **209**, 508–514.
55 J. Sun, Q. Liang, Q. Han, X. Zhang and M. Ding, *Talanta*, 2015, **132**, 557–563.
56 G. Kyzas, N. Travlou, O. Kalogirou and E. Deliyanni, *Materials*, 2013, **6**, 1360–1376.
57 S. Pu, S. Xue, Z. Yang, Y. Hou, R. Zhu and W. Chu, *Environ. Sci. Pollut. Res.*, 2018, **25**, 17310–17320.
58 J. Su, M. Cao, L. Ren and C. Hu, *J. Phys. Chem. C*, 2011, **115**, 14469–14477.
59 X. Wang, J. Lu, B. Cao, X. Liu, Z. Lin, C. Yang, R. Wu, X. Su and X. Wang, *Colloids Surf., A*, 2019, **560**, 384–392.
60 A. Dubey, N. Bhavsar, V. Pachchigar, M. Saini, M. Ranjan and C. L. Dube, *Ceram. Int.*, 2022, **48**, 4821–4828.
61 R. Kumar, S. M. Youssry, E. Joanni, S. Sahoo, G. Kawamura and A. Matsuda, *J. Energy Storage*, 2022, **56**, 105896.
62 M. H. Kahsay, N. Belachew, A. Tadesse and K. Basavaiah, *RSC Adv.*, 2020, **10**, 34916–34927.
63 M. S. Akhtar, S. Fiaz, S. Aslam, S. Chung, A. Ditta, M. A. Irshad, A. M. Al-Mohaimeed, R. Iqbal, W. A. Al-onazi, M. Rizwan and Y. Nakashima, *Sci. Rep.*, 2024, **14**, 18172.
64 S. S. Banerjee and D.-H. Chen, *Chem. Mater.*, 2007, **19**, 6345–6349.
65 X. Zhang, G. Yi, Z. Zhang, J. Yu, H. Fan, P. Li, H. Zeng, B. Xing, L. Chen and C. Zhang, *Environ. Sci. Pollut. Res.*, 2021, **28**, 14671–14680.
66 F. Sadegh, N. Politakos, E. González De San Román, O. Sanz, I. Perez-Miqueo, S. E. Moya and R. Tomovska, *RSC Adv.*, 2020, **10**, 38805–38817.
67 A. E. Oral, S. Aytas, S. Yusan, S. Sert, C. Gok and O. Elmastas Gultekin, *Anal. Lett.*, 2020, **53**, 1812–1833.
68 Z. Dai, Y. Sun, H. Zhang, D. Ding and L. Li, *J. Chem. Eng. Data*, 2019, **64**, 5797–5805.
69 G. Lujanienė, R. Novikau, E. F. Joel, K. Karalevičiūtė, S. Šemčuk, K. Mažeika, M. Talaikis, V. Pakštas, S. Tumėnas, J. Mažeika and K. Jokšas, *Molecules*, 2022, **27**, 8035.
70 Y. Shan, X. Y. Xu, K. Z. Chen and L. Gao, *Adv. Mater. Res.*, 2013, **774–776**, 532–535.
71 Z. Monsef Khoshhesab, Z. Ayazi and M. Dargahi, *Int. J. Nanosci. Nanotechnol.*, 2020, **16**, 35–48.
72 Y. Zhao, L. Zhang, Z. Chu, Z. Xiong and W. Zhang, *Anal. Methods*, 2017, **9**, 443–449.

73 A. Yang, Y. Zhu, P. Li and C. P. Huang, *Sci. Rep.*, 2019, **9**, 6471.
74 A. S. Kuzenkova, A. Y. Romanchuk, A. L. Trigub, K. I. Maslakov, A. V. Egorov, L. Amidani, C. Kittrell, K. O. Kvashnina, J. M. Tour, A. V. Talyzin and S. N. Kalmykov, *Carbon*, 2020, **158**, 291–302.
75 N. L. Tuyen, T. Q. Toan, N. B. Hung, P. Q. Trieu, N. N. Dinh, D. B. Do, D. Van Thanh and V.-T. Nguyen, *RSC Adv.*, 2023, **13**, 7372–7379.
76 N. Li, H.-L. Jiang, X. Wang, X. Wang, G. Xu, B. Zhang, L. Wang, R.-S. Zhao and J.-M. Lin, *TrAC, Trends Anal. Chem.*, 2018, **102**, 60–74.
77 T. Zhang, X. Gao, J. Li, L. Xiao, H. Gao, F. Zhao and H. Ma, *Def. Technol.*, 2024, **31**, 95–116.
78 L. Q. Vo, A.-T. Vu, T. D. Le, C. D. Huynh and H. V. Tran, *ACS Omega*, 2024, **9**, 17506–17517.
79 M. Hammad, P. Fortugno, S. Hardt, C. Kim, S. Salamon, T. C. Schmidt, H. Wende, C. Schulz and H. Wiggers, *Environ. Technol. Innovation*, 2021, **21**, 101239.
80 L. Xu and J. Wang, *Crit. Rev. Environ. Sci. Technol.*, 2017, **47**, 1042–1105.
81 W. Tu and W. Cai, *Toxics*, 2024, **12**, 447.
82 R. Jain, *Appl. Water Sci.*, 2025, **15**, 223.
83 S.-Y. Hsu, S.-C. Lin, J.-A. Wang, C.-C. Hu, C.-C. M. Ma and D.-H. Tsai, *Electrochim. Acta*, 2019, **296**, 427–437.
84 N. L. Tuyen, T. Q. Toan, N. B. Hung, P. Q. Trieu, N. N. Dinh, D. B. Do, D. Van Thanh and V.-T. Nguyen, *RSC Adv.*, 2023, **13**, 7372–7379.
85 W. Lu, L. Li, D. Ding, Z. Dai, S. Tang, C. Cao, L. Liu and d T. Chen, *J. Nanosci. Nanotechnol.*, 2018, **18**, 8160–8168.
86 A. A. Kadam, J. Jang and D. S. Lee, *Bioresour. Technol.*, 2016, **216**, 391–398.
87 H. Elhaes, A. Ibrahim, O. Osman and M. A. Ibrahim, *Sci. Rep.*, 2024, **14**, 14825.
88 A. S. El-Sheikh, N. S. Abdelaziz, K. S. Amin, H. Elhaes and M. A. Ibrahim, *Sci. Rep.*, 2025, **15**, 28905.
89 T. T. N. Le, V. T. Le, M. U. Dao, Q. V. Nguyen, T. T. Vu, M. H. Nguyen, D. L. Tran and H. S. Le, *Chem. Eng. Commun.*, 2019, **206**, 1337–1352.
90 H. C. Vu, A. D. Dwivedi, T. T. Le, S.-H. Seo, E.-J. Kim and Y.-S. Chang, *Chem. Eng. J.*, 2017, **307**, 220–229.
91 B. Fadeel, C. Bussy, S. Merino, E. Vázquez, E. Flahaut, F. Mouchet, L. Evariste, L. Gauthier, A. J. Koivisto, U. Vogel, C. Martín, L. G. Delogu, T. Buerki-Thurnherr, P. Wick, D. Beloin-Saint-Pierre, R. Hischier, M. Pelin, F. Candotto Carniel, M. Tretiach, F. Cesca, F. Benfenati, D. Scaini, L. Ballerini, K. Kostarelos, M. Prato and A. Bianco, *ACS Nano*, 2018, **12**, 10582–10620.